

Scotland's Rural College

MXene-Based Nanomaterials for Biomedical Applications: Healthier Substitute Materials for the Future

Siwal, Samarjeet Singh; Kaur, Harjot; Chauhan, Gunjan; Thakur, Vijay Kumar

Published in:
Advanced NanoBiomed Research

DOI:
[10.1002/anbr.202200123](https://doi.org/10.1002/anbr.202200123)

First published: 04/12/2022

Document Version
Publisher's PDF, also known as Version of record

[Link to publication](#)

Citation for published version (APA):

Siwal, S. S., Kaur, H., Chauhan, G., & Thakur, V. K. (2022). MXene-Based Nanomaterials for Biomedical Applications: Healthier Substitute Materials for the Future. *Advanced NanoBiomed Research*, [2200123]. <https://doi.org/10.1002/anbr.202200123>

General rights

Copyright and moral rights for the publications made accessible in the public portal are retained by the authors and/or other copyright owners and it is a condition of accessing publications that users recognise and abide by the legal requirements associated with these rights.

- Users may download and print one copy of any publication from the public portal for the purpose of private study or research.
- You may not further distribute the material or use it for any profit-making activity or commercial gain
- You may freely distribute the URL identifying the publication in the public portal ?

Take down policy

If you believe that this document breaches copyright please contact us providing details, and we will remove access to the work immediately and investigate your claim.

MXene-Based Nanomaterials for Biomedical Applications: Healthier Substitute Materials for the Future

Samarjeet Singh Siwal, Harjot Kaur, Gunjan Chauhan, and Vijay Kumar Thakur*


MXene-based nanomaterial is a revolution 2D material achieving outstanding scientific attention owing to its universal characteristics for different applications (such as electronic appliances, power production, sensors, drug transfer, and biomedical). Although, the cytotoxic consequences of MXene have a considerable circumstance. Thus, rigorous investigation of the biocompatibility of MXene is a crucial prerequisite, formerly the preface to the human biological approach. Literature reveals functional outcomes wherever MXenes are used in vitro and in vivo cancer representatives. It affects drug transfer methods, sensing electrodes, and assisting mechanisms for photothermal treatment and hyperthermy techniques. In this review, the synthesis process (such as top-down and bottom-up approaches) and properties (such as mechanical, electrical, optical, oxidative/thermal stability, and magnetic) of MXene-based nanomaterials (NMs) are discussed. In addition, the different applications (such as tissue engineering, cancer theranostic, and other biomedical [such as drug delivery biosensors and surface-enhanced Raman spectroscopy substrates for biomedical applications], antiviral, and immunomodulatory properties against SARS-CoV-2) of MXene-based NMs are discussed in detail. Finally, the conclusion, existing challenges, and future outlooks are highlighted for more scope in this field.

S. S. Siwal, H. Kaur, G. Chauhan
Department of Chemistry
M.M. Engineering College
Maharishi Markandeshwar (Deemed to be University)
Mullana-Ambala, Haryana 133207, India

V. K. Thakur
Biorefining and Advanced Materials Research Center
Scotland's Rural College (SRUC)
Kings Buildings, West Mains Road, Edinburgh EH9 3JG, UK
E-mail: Vijay.Thakur@sruc.ac.uk

V. K. Thakur
School of Engineering
University of Petroleum & Energy Studies (UPES)
Dehradun, Uttarakhand 248007, India

V. K. Thakur
Centre for Research & Development
Chandigarh University
Mohali, Punjab 140413, India

 The ORCID identification number(s) for the author(s) of this article can be found under <https://doi.org/10.1002/anbr.202200123>.

© 2022 The Authors. Advanced NanoBiomed Research published by Wiley-VCH GmbH. This is an open access article under the terms of the Creative Commons Attribution License, which permits use, distribution and reproduction in any medium, provided the original work is properly cited.

DOI: 10.1002/anbr.202200123

1. Introduction

The Gogotsi group discovered the first titanium carbide MXene (Ti_3C_2) at Drexel University in 2011.^[1] After that, MXenes have persisted in obtaining growing attraction from investigators owing to their graphene-like characteristics. It also has better conduction, hydrophilicity, an elevated superficial area, better mechanical stability, and photothermal transformation effects for different applications.^[2] The remarkable results allowed MXenes to discover possible applications within energy transformation, storage, catalysis, biocidal films, and the biomedical domain.^[3] MXene is a 2D material generally designed through biochemical etching of a bulk stage comprehended as a MAX segment. “M” denotes an initial transition metallic, “A” indicates an element of group 13 or 14, and X marks carbon or nitrogen.

Their distinctive electronic networks and high superficial areas create 2D substances capable of numerous electric and energy utilization. Therefore, the preparation, characteristics, and implementations of unique 2D substances have developed into one of the multiple stimulating fields of attention within science and technology. Single coatings of graphene (Gr),^[4] boron nitride (BN),^[5] transition metal dichalcogenides (TMDs),^[6] and phosphorene were effectively received from their substance van der Waals-coated networks.^[7] Newly, it has been demonstrated that through utilizing an assortment of chemical peeling and sonication, the preparation and mass manufacture of 2D materials from 3D-coated complexes by chemical bonding among the coatings are also possible. In this respect, it has been shown that using hydrofluoric acid (HF) media and sonication, a few components of the MAX phase family may be exfoliated within 2D transition metal carbide (TMC) and nitride coatings, named MXenes.^[8]

Recently, MXenes, which have been investigated for numerous chemically and biomedically utilizations, are restricted to Ti_2CT_x , $\text{Ti}_3\text{C}_2\text{T}_x$, tantalum carbide MXene ($\text{Ta}_4\text{C}_3\text{T}_x$), and niobium carbide MXene (Nb_2CT_x). Among these MXene brood components, $\text{Ti}_3\text{C}_2\text{T}_x$ is the considerable thoroughly studied MXene owing to the simple preparation methods. The appealing characteristics of MXene are suitable near-infrared (NIR) preoccupation that is useful for theranostics, photothermal treatment, and synergetic cancer remedy.^[9] MXenes also have antimicrobial effects and are used in mesh films.^[10] In addition, MXenes have

also been involved as biosensors^[11] and for bioimaging after being transformed within quantum dots (QDs).^[12]

Here in this review article, we have tried to summarize all the insight views on the synthesis process (such as top-down and bottom-up approaches) and properties (such as mechanical, electrical, optical, oxidative/thermal stability, and magnetic) of MXene-based NMs. In addition, the different applications (such as tissue engineering, cancer theranostic, and other biomedical (such as drug delivery biosensors and surface-enhanced Raman spectroscopy [SERS] substrates for biomedical applications, antiviral, and immunomodulatory properties against SARS-CoV-2) of MXene-based NMs have been discussed in detail. Finally, the conclusion, existing challenges, and future outlooks are highlighted for more scope in this field.

2. The Synthesis Process of MXene-Based Nanomaterials

The first synthesized MXene NMs is Ti_3C_2 . This 2D substance is synthesized by eliminating Al particles from titanium–aluminum carbide (Ti_3AlC_2) powder using an exfoliation process in an HF solution. Mostly there are two kinds of methods utilized in the preparation of MXenes NMs:^[13] 1) top-down approach and 2) bottom-up approach.

Previously, MXene nanosheets were instantly exfoliated from the bulk substantial within an HF as a solution. In contrast, chemical vapor deposition (CVD) and wet chemical methods are the broadly assumed processes in the latter. Usually, the bottom-up approach is utilized for bulk constituents that are not very calm to exfoliate.^[14]

Yang et al.^[15] developed a 2D Nb_2C MXene titanium plate ($Nb_2C@TP$)-based clinical implant with functional multimodal anti-infection processes. The incorporation procedure of ultrathin 2D Nb_2C nanosheets (NSs) is shown within **Figure 1a**. Transmission electron microscopy (TEM) pictures showed the standard planar topology of Nb_2C NSs with an average dimension of ≈ 150 nm (Figure 1b,c). Selected-area electron diffraction (SAED) designs delivered the maintained well-defined polycrystalline configuration, confirming the successful preparation of Nb_2C MXene (Figure 1d). In contrast, it determined the exact arrangement of Nb_2C NSs with an energy-dispersive spectrometer (EDS) study that demonstrated consistent diffusion of Nb and C elements within the 2D MXene planar configuration (Figure 1e). The scanning electron microscope (SEM) pictures revealed the soft cloud-like configuration of $Nb_2C@TP$, and higher-magnification photos showed a fish scale-shaped surface (Figure 1f). Elemental mapping and EDS curve (Figure 1g) demonstrated that $Nb_2C@TP$ s were beneath a surface range of Nb and C components, leading to the booming binding of Nb_2C MXene to TP support. Also, Raman spectra show the standard ω_1 and ω_4 vibration ways after incorporating Nb_2C NSs onto TP support (Figure 1h). X-ray photoelectron spectroscopy (XPS) was utilized to define the arrangement and surface endings of $Nb_2C@TP$ (Figure 1i). To assess the photothermal transformation efficacy of $Nb_2C@TP$, $Nb_2C@TP$ beneath NIR laser radiation with a high-power density shows a steady heat ridge up to 70 °C in 2 min (Figure 1j). Similarly, to additionally examine the laser-induced photothermal resilience of $Nb_2C@TP$, they

detected the recycling temperature deviations of $Nb_2C@TP$ beneath a NIR laser. The photothermal activity of $Nb_2C@TP$ did not achieve evident degeneration during five laser on/off processes (Figure 1k), emphasizing the incredible photothermal execution of $Nb_2C@TP$ within the potential continued photothermal removal of bacteria.

2.1. Top-Down Approach

The top-down approach depends upon the immediate flaking of bulk crystals that uses different pouring strengths, such as automatic and biochemical exfoliations. The broad emphasis of MXenes' incorporation is upon fluid-phase exfoliation, a simple and better-outcome approach established to be highly effective in producing ultrathin, nanorange MXenes (**Figure 2a**). The conversion from parent MAX-phase ceramics (Figure 2b–d) to nanorange 2D MXenes experiences the subsequent two stages: 1) in this stage, delamination through HF etching to get multicoated-stacked MXenes (Figure 2e–g) and 2) here, the corrosion through organic base molecules' embolism or electrode sonication cracking develops few-film or solitary-film MXenes (Figure 2h–j). Benefitting from this process, almost all kinds of MXenes would be acquired with expanded surfaces of few- or single-film nanofilms, containing nanoscale-adjacent dimensions and atomic-range consistency.^[16]

2.1.1. Advantages and Disadvantages of MXene-Based NMs Synthesized by Top-Down Approach^[17]

Advantages: 1) They can be synthesized at room temperature; they can undergo. 2) large-scale production; and 3) utilize abundant raw material

Disadvantages: 1) They have low production yield; and 2) generally, the sizes of the produced sheets are large that lead to various issues in biomedical applications such as low therapeutic outcome, biosafety issues, and are not suitable for intravenous administration.

2.2. Bottom-Up Method

The bottom-up methods are the substitutive approach to constructing 2D NMs through the atomic range, managing their arrangement and morphology. It would simulate 2D nanomaterials that were difficult to get through natural peeling from bulk. CVD growth^[18] and wet chemical amalgamation^[19] are the main synthetic methods based on the bottom-up approach to design layered substances with an increased manufacturing rate. Compared with the standard 2D constituents, the recent advancements of a bottom-up process to manufacture MXenes are still thriving, possibly due to the intricate particles and arrangements of MXenes' in-layer surface.

CVD^[20] and hydro- or solvothermal method^[19a,19c] are the two primary synthetic processes based upon the bottom-up strategy. Lee et al.^[18a] found that they would incorporate single-film MoS_2 layers upon amorphous SiO_2 supports with MoO_3 and S precipitates as precursors through the CVD method at 650 °C. Nevertheless, the CVD process cannot be suitable for tailoring 2D nanofilms with a small film dimension for oncologic

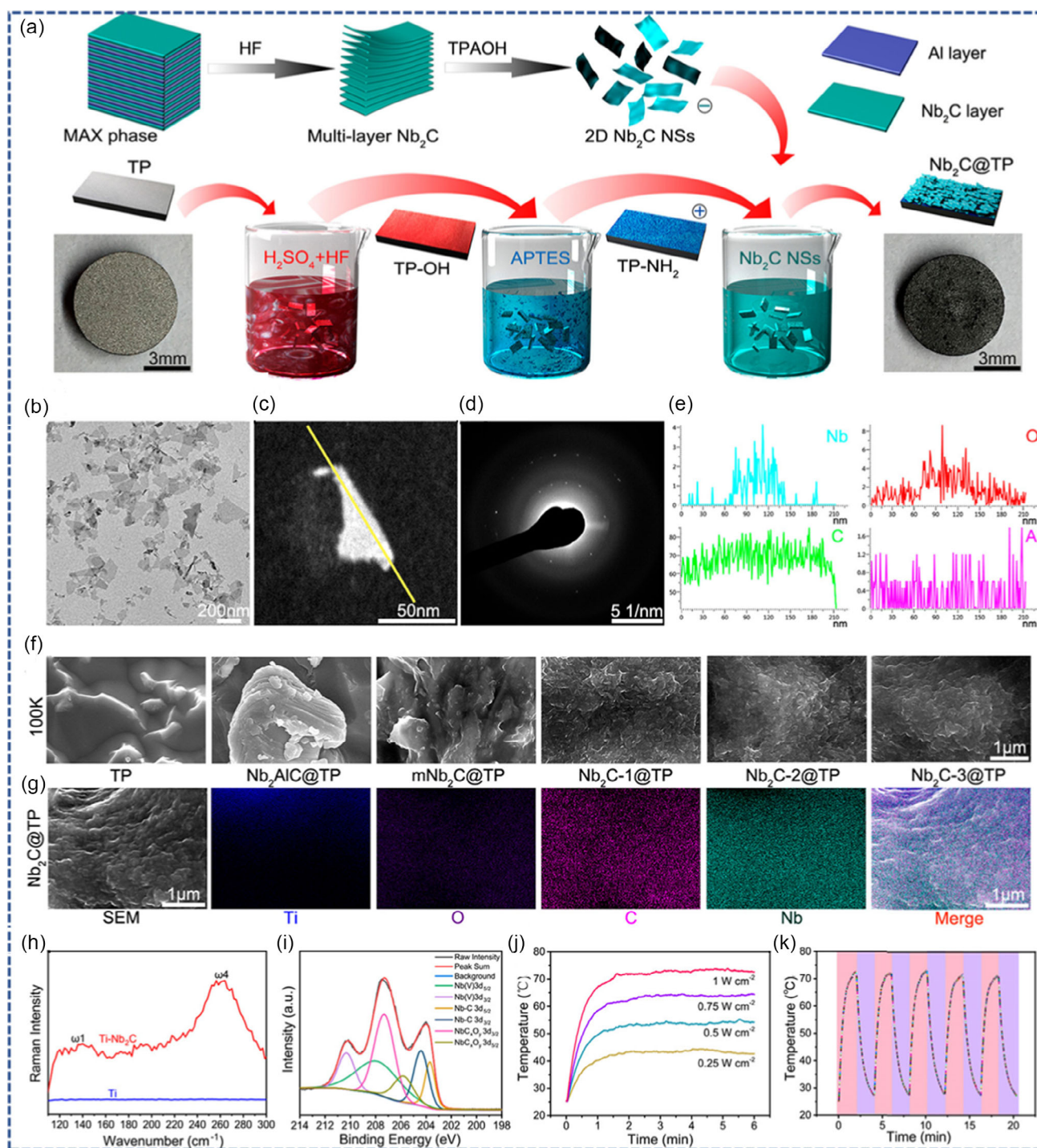


Figure 1. Synthesis and characterization of Nb₂C@TP. a) Schematic description of the preparation techniques for Nb₂C@TP. b) TEM picture of Nb₂C NSs. c) Bright-field TEM and d) SAED pictures. e) EDS linear-scanning curve of Nb₂C NSs for Nb, C, O, and Al components of (c). f) SEM picture of TP, Nb₂AlC@TP, mNb₂C@TP, and Nb₂C@TP. g) SEM elemental mapping of Nb₂C@TP. h) Raman spectrum of TP and Nb₂C@TP. i) High-resolution XPS curve of Nb component for Nb₂C@TP. j) Photothermal arcs of Nb₂C@TP under 808 nm laser radiation of distinct power density. k) Heating arcs of Nb₂C@TP for five laser on/off processes. Reproduced with permission.^[15] Copyright 2021, American Chemical Society.

utilization. Preparation in a high-temperature media with a manageable synthetic approach is a universal bottom-up method for

synthesizing 2D nanofilms with finely controlled size, surface, and arrangement.

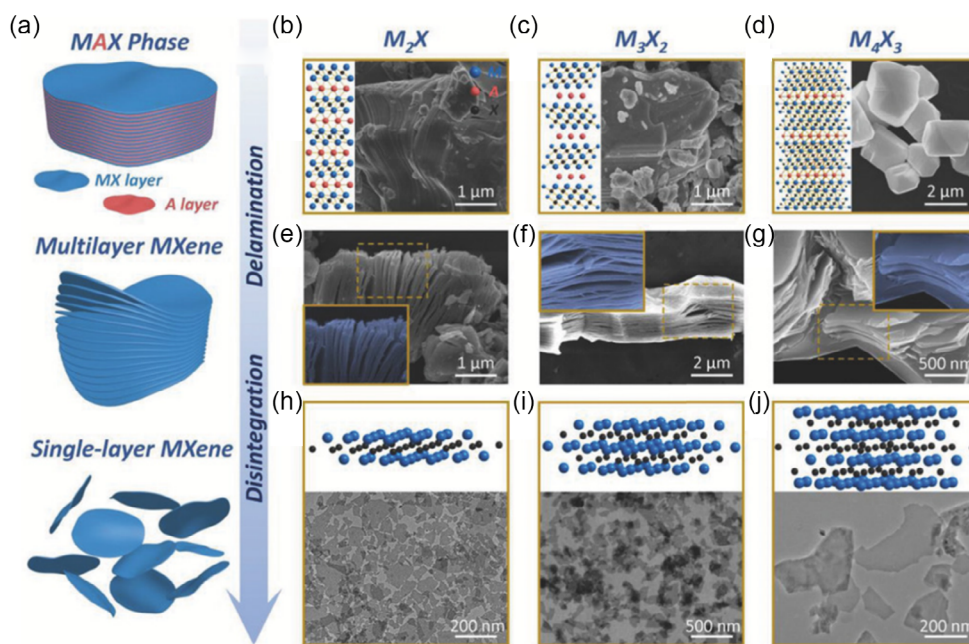


Figure 2. Synthetic ways of MXenes for biomedicine. a) The graphic display for the preparation of biocompatible MXenes, with HF etching (delamination), organic base particles embolism (breakdown), and exterior functionalization by organic particles or inorganic NPs (superficial transformation). b) 2D ball-and-stick standards and SEM pictures of reactant MAX phase for M_2X , e) SEM picture of multicoated M_2X , and h) 3D ball-and-stick samples and TEM picture single-film M_2X -based MXenes. c) 2D ball-and-stick samples and SEM pictures of antecedent MAX stage for M_3X_2 , f) SEM picture of multilayer M_3X_2 , and i) 3D ball-and-stick samples and TEM picture single-film M_3X_2 -based MXenes. d) 2D ball-and-stick models and SEM pictures of precursor MAX phase for M_4X_3 , g) SEM picture of multilayer M_4X_3 , and j) 3D ball-and-stick samples and TEM picture solitary-film M_4X_3 -based MXenes. Reproduced with permission.^[16] Copyright 2018, John Wiley and Sons.

A large portion of 2D inorganic NMs has been prepared via this process and utilized in cancer theranostics. It achieves an exemplary bottom-up method of biocompatible polyethylene glylated (PEGylated) MoS_2 nanofilms via solvothermal processing for admirably effective photothermal degeneration of tumors (Figure 3a). Besides the conventional up-down process for manufacturing 2D MoS_2 nanofilms by liquid exfoliation from bulk MoS_2 , the efficient and universal bottom-up single-pot synthesis technique gives the nanosheets intrinsic colloidal resilience in biological circumstances able to manage critical mechanical and structural constraints. Particulate dimensions variation and consistency of PEGylation can considerably improve the photothermal transformation efficacy of nanofilms for more promising cancer treatment. Based on the worth of synthetic methodologies using the bottom-up process and their novel synthetic chemistry, a simple single-pot synthesis method for simulating a 2D MoS_2/Bi_2S_3 compound theranostic nanosystem for multimodal tumor imaging-guided photothermal and synergistic radio treatment (Figure 3b) is suggested.^[21]

2.2.1. Advantages and Disadvantages of MXene-Based NMs Synthesized by Bottom-Up Approach^[17]

Advantages Include: 1) morphology control; 2) easier functionalization; and 3) adequate atomic utilization.

Disadvantages Include: 1) efficient and low-toxicity precursors that still need to be considered; 2) mild reaction conditions and monodispersity; and 3) need of large-scale production.

3. Properties of MXene-Based Nanomaterials

MXene has two-layered carbon or nitrogen units, V_2C , Ti_2C , Nb_2C_1 , and 32 layered carbon–nitrogen factions, as Ti_3C_2 and Ti_3CN , and 43 layered networks as Nb_4C_3 , Ta_4C_3 etc. This layered design suggests unusual effects; they may exhibit metallic, semi-metallic, and conducting shielding characteristics. Simultaneously, it may be stretchy, rigid, and heat resilient as ceramic substances. MXenes exhibit increased surface activity, hydrophilic character, and adsorption capability owing to their enormous surface area. MXene-based NMs generally are utilized in different areas such as energy storage, triboelectric nanogenerators, optoelectronic appliances, wastewater processing, gas sensors, electromagnetic interference (EMI) shielding, medicine, etc.^[12a,14,22]

Yet, because of their moderately lower extermination constants and photothermal modification efficacies within the NIR bio window, their photothermal effectiveness is not elevated sufficiently to accomplish expected therapeutic results. Hence, developing new 2D nanofilms with promising photothermal execution is necessary.

Among the eminent characteristics of MXene, the utmost scope of Young's modulus, tunable bandwidth, and improved electric and thermal conduction is considered exceptional and valuable. Remarkably, the hydrophilic character integrated with improved thermal conduction of MXenes distinguishes them from other 2D substances with graphene.^[23] Finally, it may adjust the related characteristics and expulsive executions through 1) arrangement, 2) morphology functionality, and 3) surface/geometric design connections.

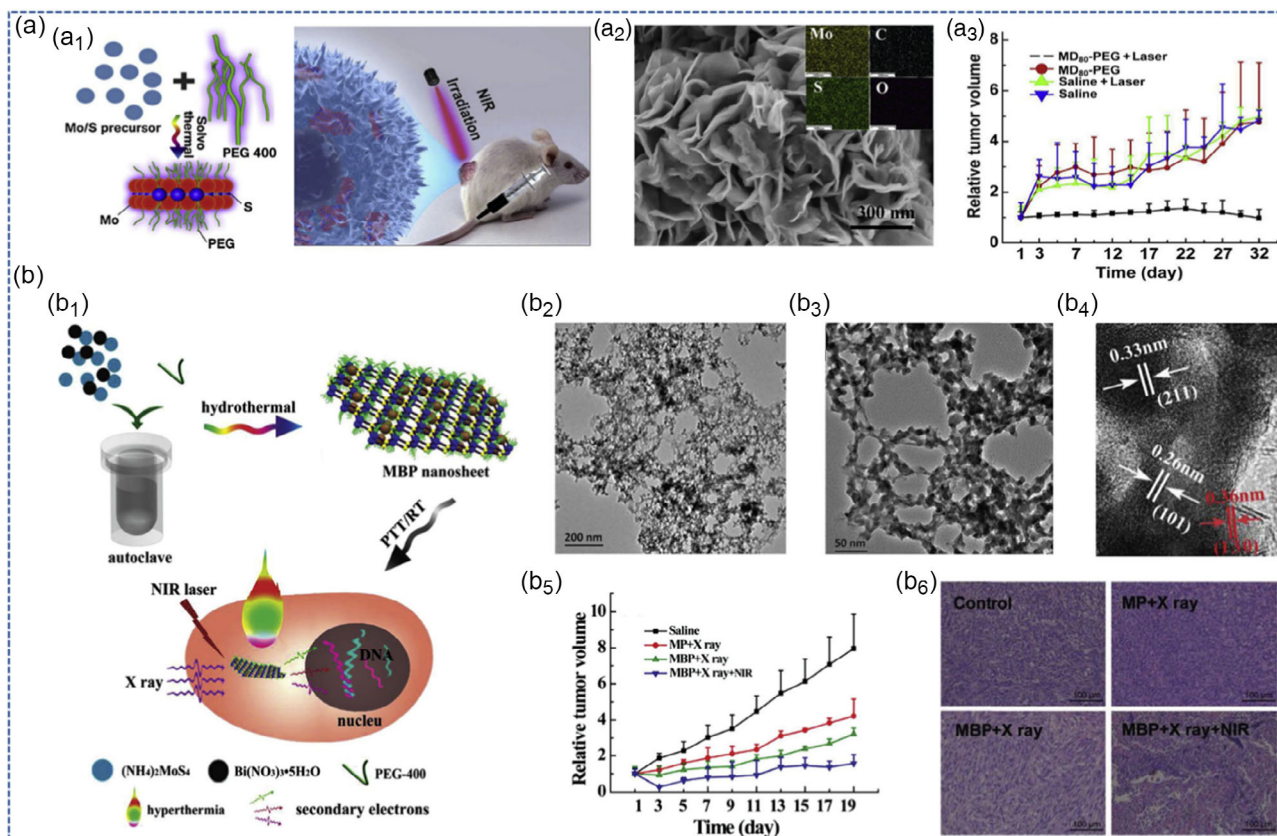


Figure 3. Synthesis of 2D inorganic nanofilms through bottom-up methods. a) Preparation of PEGylated MoS₂ nanofilms by bottom-up approach for extremely effective photothermal deterioration of the tumor. a₁) Graphic explanation of the solvothermal preparation process of MoS₂-PEG nanofilms. a₂) Shows the field-emission SEM (FESEM) picture of MoS₂-polyethylene glycol (MoS₂-PEG). Insets show the related elemental mappings of Mo, S, C, and O. a₃) Time-reliant tumor-advancement arcs after different therapies, as noted within the sculpture. b) Simple single-step preparation of a 2D MoS₂/Bi₂S₃ compound theranostic nanosystem or multimodal cancer theranostics. b₁) Graphic representation of the solvothermal preparation of MoS₂/Bi₂S₃-PEG material nanofilms and corresponding photothermal and radio synergetic treatment. b₂ and b₃) TEM pictures of MoS₂/Bi₂S₃-PEG-synthesized nanosheets at lower (b₂) and increased (b₃) amplifications. b₄) High-resolution TEM (HRTEM) picture of MoS₂/Bi₂S₃-PEG hybrid nanofilms. b₅) Time-reliant tumor-advancement arcs after different remedies as noted within the figure (*n* = 6). b₆) H&E discoloration for compulsive modifications into tumor tissues from per assembly. Reproduced with permission.^[21] Copyright 2018, Elsevier Ltd.

3.1. Mechanical Properties

Due to more powerful M–N and M–C interactions, the mechanical characteristics of MXenes are considerably more curious. The previous investigation completed upon simulation has suggested flexible limits to be two times higher than MAX designs and 2D segments like CdS₂. The elastic effects are 2–3 times more inferior than Gr; their bending feature (1050 GPa) is the highest, ensuring their use as mixed-support composites. MXenes have an incredible interaction capability with polymeric matrix than graphene for compound utilities due to the active functionalities.^[24]

Thus, new practical findings should improve the preparation process to define its deficiency arrangement and differentiate different active groups of new segments.^[25] Maybe, an entire assessment of mechanical characteristics and prominent efficient groups established upon theory and investigations is still to be found.

MXenes are seductive drug deliverers because of their high exterior area. Absorption and functionalization with hydrogel support MXenes with enhanced doxorubicin (DOX)-supporting

capacity for a blend with chemotherapy and photothermal excision of cancer.^[10a,26] Likewise, the mechanical characteristics of Ti₃C₂/polyacrylamide nanocomposite (PAM NC) hydrogels use Ti₃C₂ as a crosslinker toward in situ free-radical polymerization, which can be enhanced by enhancing the concentration of Ti₃C₂, that is essential for a strong and durable system.^[27] Despite stretching and extreme condensation, Ti₃C₂/PAM NC hydrogels did not show ruptures and healed without a contraction force. Similarly, utilizing chloramphenicol as a standard drug, the honeycomb-type design and superior swelling capability of Ti₃C₂/PAM NC hydrogels demonstrated assurance as transportation, with percentage liberation matters and drug loadings that were more elevated compared with conventional organic cross-linked BIS/PAM hydrogels.^[28]

3.2. Electrical Properties

Two essential characteristics beneath the main problem to MXenes are the electronic and electric effects. It can adjust these

by changing its operating groups, material corrective, or solid-solution construction.^[29] The electrical conductivities related to packed sheets of MXenes coincided with graphene multilayers. They were more significant than carbon nanotubes (CNTs)^[30] and reduced graphene oxide (rGO) materials.^[31] Further, resistivity increments with different coatings and restrictions of active molecules are shown. Owing to this, the conductivities of pretending positions have utmost significance over practical observances.^[32]

Meanwhile, some practical outcomes demonstrate that MXenes shift within semiconductors by exterior functionalization. For instance, **Figure 4** illustrates the projected density of states (PDOS) and the possible band configurations of Ti_2CT_x with distinct stops. Additionally, it is shown that $-F$ and $-OH$ have equivalent consequences on the electronic effects of MXenes. Subsequently, they take a single electron in the symmetry condition. At the same time, O terminations exhibit various outcomes later. Their oxidation conditions allow the approval of two electrons.^[33]

It is also shown that the electronic effects of MXenes are particularly affected by M and X elements.^[2a] For example, MXenes with elevated atomic numbers are expected to be topologic heat proofing,^[24] while plain Ti_3C_2 shows metal effects.^[34] Meanwhile, nitrogen contains more electrons, and carbonitride and nitride MXenes show much more powerful metallic characteristics than carbide MXenes.

3.3. Optical Characteristics

The UV-vis rays spectrum absorption is critical for photovoltaic, photocatalytic, translucent, and optically instructing electrode devices. Films of $Ti_3C_2T_x$ may fascinate light energy into the UV-vis part from a wavelength between 300 and 500 nm. The complete experimentation procedure is illustrated in **Figure 5a**. **Figure 5b** exhibits the microstructure of multicoated MXene, which is already gone through ultrasonic processing. **Figure 5c,d** illustrates the microstructure of the multilayer

MXene fragments after ultrasonic cure. The microscopic surface of the flower-type NiCo layered double oxide (NiCo-LDH) is depicted in **Figure 5e**; the flower-type arrangement of NiCo-LDH comprises a few display networks. **Figure 5f-i** shows the configuration of NiCo-LDH/MXene mixtures with various incorporations of MXene. The external surface of NiCo-LDH/MXene-1 is depicted in **Figure 5e**. The MXene flake is secured through the extensive NiCo-LDH while the doped MXene in this mixture is 50 wt%. **Figure 5g** shows the NiCo-LDH/MXene-2 representative, and the incorporation of MXene within this specimen is 66 wt%. Though the ratio of NiCo-LDH upon the exterior of the specimen is at an elevated level, it may also follow the MXene flakes beneath NiCo-LDH. As the doped of MXene persists rising, when it reaches 75 wt%, NiCo-LDH flowers squeeze in between the MXene coatings into the NiCo-LDH/MXene-3 trial (**Figure 5h**). The network like this is additionally facilitative to the contemplation and distribution of electromagnetic waves (EMW), and it may facilitate the absorption and excess of EMW. While the load of MXene rises to 80 wt%, the flower-type arrangement of NiCo-LDH is not apparent, and the display system manages to be affixed to the MXene films (**Figure 5i**).^[35]

Actual 10 nm sheet consistency registered transmission of 91%. Further, it may get a broad and robust absorption band of about 700–800 nm, which depends on sheet viscosity, showing the appearance of light green films, which allow it to be entirely helpful in photothermal treatment uses.^[36] Remarkably, it would improve the transmission proportion by varying its width and ion intercalation.

3.4. Thermal Steadiness

The critical parameter to be comprehensively observed is the strength that affects the existence of water/oxygen in the preparation of MXenes. Concerning DFTs' compact binding estimates, the earlier results showed that carbohydrates' hydroxylated ingredients and uneven dispersals of C/N were

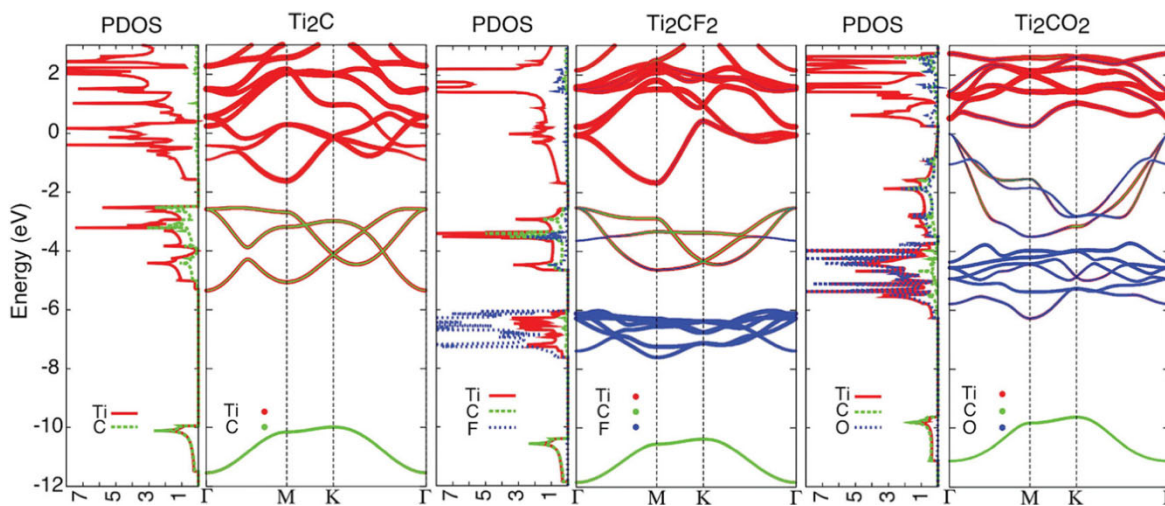


Figure 4. Density functional theory (DFT) forecasts of electronic effects of Ti_2CT_x with distinct endings: PDOS and band arrangements. Reproduced with permission.^[33] Copyright 2020, American Chemical Society.

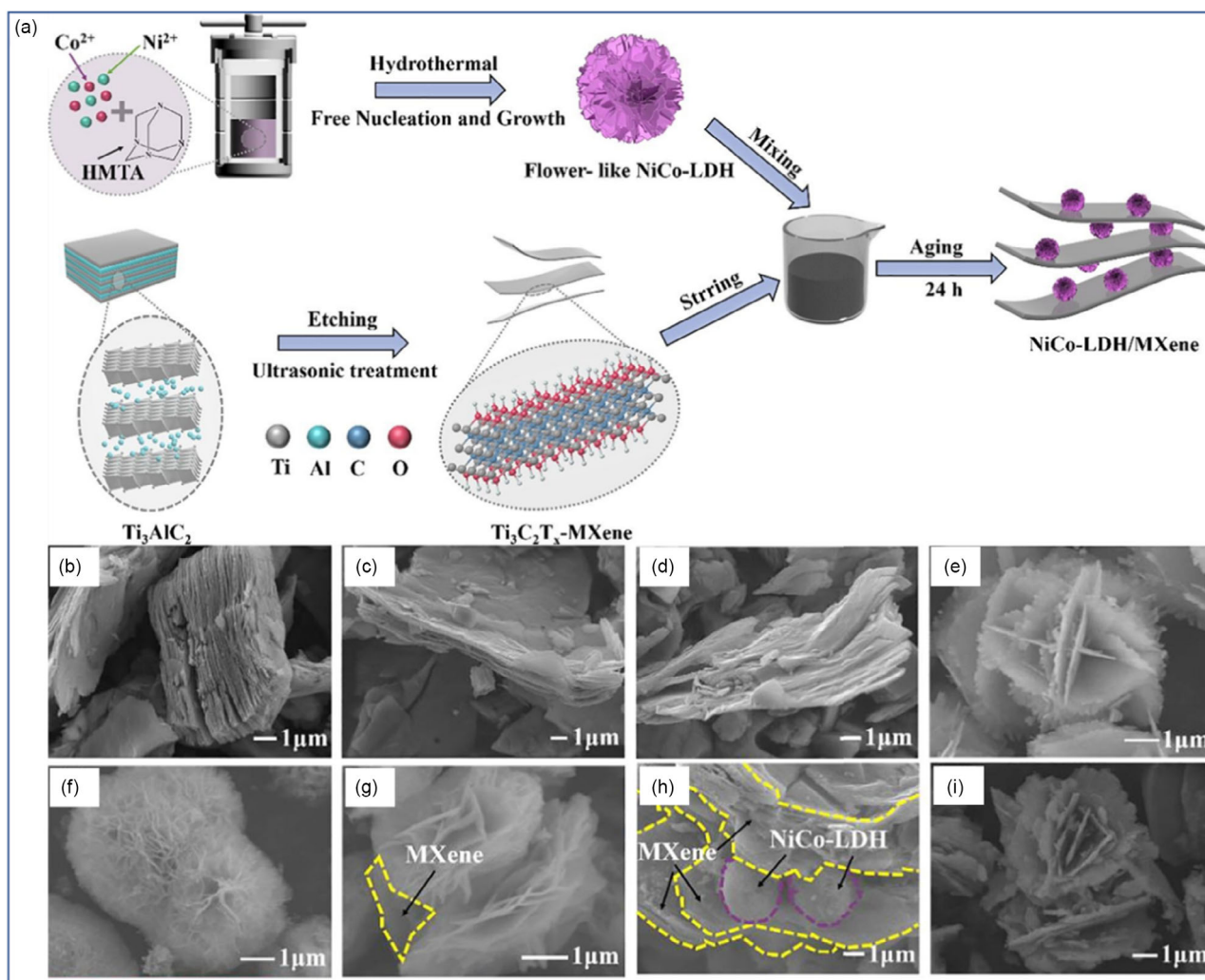


Figure 5. a) The key synthesis procedure of NiCo-LDH/MXene amalgams. SEM pictures of MXene (a–c), NiCo-LDH (d), NiCo-LDH/MXene (NiCo-LDH/MXene-1 e), NiCo-LDH/MXene-2 f), NiCo-LDH/MXene-3 g), NiCo-LDH/MXene-4 h). Reproduced with permission.^[35] Copyright 2021, Elsevier Ltd.

susceptible to possessing the highest steadiness and being thermodynamically favorable. During experimental investigation, new MXenes decay through oxidation under extended maintenance to oxygen content beneath the impact of water solution at more high heat or UV radiation orientation to air.^[37]

Furthermore, it can also reduce the oxidation rate kept by MXenes' colloidal media by preserving it in a shady atmosphere-supported fridge or beneath the consequence of a whole vacuum repository.

3.5. Magnetic Properties

However, numerous 2D substances have been discovered; most are nonmagnetic, limiting their utilization in spintronics. Hence, the purpose of steady magnetism in 2D has been a long-desired objective. Remarkably, some new MXenes, such as Ti_2C , Ti_2N , Cr_2C , Cr_2N , and Mn_2C , are estimated to be inherent magnetic ingredients. Among them, Ti_2C ,^[38] Ti_2N ,^[32] and Cr_2C ^[39] are ferromagnetic, whereas Mn_2C ^[40] is antiferromagnetic. A newly

growing concentration has been expanded to magnetic MXenes with half-metallicity. In contrast, the additional spin channel is semiconducting, resulting in entirely spin-polarized electrons on the Fermi level.^[41] Surface spaces are essential in estimating the magnetic effects revealed through MXene-based NMs. It shows that rigid covalent connections occur between M and X, and the superficial functionalities that generate considerably MXene features are nonmagnetic.

Similarly, MXene substances show magnetic character due to the addition within the electron density around the Fermi area related to *d*-group orbitals shown in transition components. Surface in-plane space is adequate to ascribe potential covalent links like M–A and M–M bonds. It has also been noted that 2D chromic carbide and chromic nitride exhibit ferromagnetism, while 2D titanium nitride/carbide is identified as antiferromagnetic. The lower electron density around the Fermi area resulted from superficial spaces due to surface functionalization that could ultimately direct the disappearance of magnetic features.

4. Applications of MXene-Based Nanomaterials in the Biomedical Field

The timeline illustrating the development of MXene from 2011 to the incorporation of MXene-based aptasensor toward cancer diagnosis and therapeutics is described in **Figure 6**. The graphic for the vision of IoT-aided smartphone-based electrochemical aptasensors using MXene is depicted in **Figure 6**. Biomarkers and the aptamer using electrochemical identification methods can be a boon for early cancer diagnosis.^[42]

4.1. MXene-Based Nanomaterials for Tissue Engineering and Reforming Medication

Compared with other biomedical implementations, for example, bioimaging, tumor therapy, antibacterial, etc., MXenes have more infrequent applications within tissue engineering. The application of MXene within tissue engineering contains bone,^[43] skin,^[44] nerve,^[45] and myocardial tissue engineering^[46] principally.

MXenes have exhibited profitable prospects within material disciplines and stem cell-based tissue treatments. Thus, it can envision prospective multitasked biomedical treatments based on the remarkable benefits of MXene.^[47] One study fabricated innovative biomaterials such as Ti_3C_2 MXene nanofibers for tissue engineering and cell culture. Due to the quantity of hydrophilic functional groups, the subsequent hydrophilic compound nanofibers would be designed through electrospinning and doping.^[48] Therefore, the functional groups at the covers of MXene nanofiber compounds would deliver appropriate bionetworks for cellular development. The biochemical specimen features have been investigated through positioning bone marrow-resultant mesenchymal stem cells (BMSCs); the subsequent MXene material nanofibers showed acceptable biocompatibility and

significantly enhanced cellular movement, excluding growing the BMSCs' variation to bone-forming cells.

Surgical negligence and bone tumor reproduction are acute problems, given the remaining malicious tumor cells and the deficit of bone–tissue combination. Therefore, the reproduction and bone defect in the surgical therapy of malicious bone tumors has caused a need to produce multifunctional therapeutic stages for effectual tumor treatment and bone rejuvenation.^[49] The subsequent hybrid scaffolds had perfect features for effective photothermal modification of integrated 2D Ti_3C_2 MXene for eliciting bone-tumor removal through NIR-caused photothermal hyperthermy, executing complete tumor reduction from in vivo bone-tumor heterograft. Ti_3C_2 MXene-integrated hybrid platforms would enhance the in vivo development of developing bone tissues of the compound bioactive glass platforms; such intrinsic benefits of bone-tumor slaying and bone-tissue renewal can be perfect options for feasting bone tumors together with additional tissue engineering devices.

2D Ti_3C_2 MXenes, a unique photothermal nanoagent with special photothermal modification effects and better biocompatibility, were combined with 3D-printed bioactive glass (BG) platforms to destroy bone cancer cells and restore enormous bone deficiencies. These 2D ultrathin Ti_3C_2 NSs were incorporated via HF etching succeeding tetra propylammonium hydroxide (TPAOH) peeling of the novel bulk MAX-phase Ti_3AlC_2 ceramics (**Figure 7a**). The as-synthesized 2D Ti_3C_2 NSs would be finely disseminated in aqueous media as confirmed through the noticeable Tyndall consequence (**Figure 7b**), allowing the additional facile combination with 3D printing supports.

To assess the photothermal capability of Ti_3C_2 -BG scaffold (TBGS), we further considered a contained in vivo photothermal tumor removal using female BALB/c bared mice carrying Saos-2 bone tumor (**Figure 7c**). Photonic tumor hyperthermy functioned within the BGS + NIR and 1.0 TBGS + NIR groups,

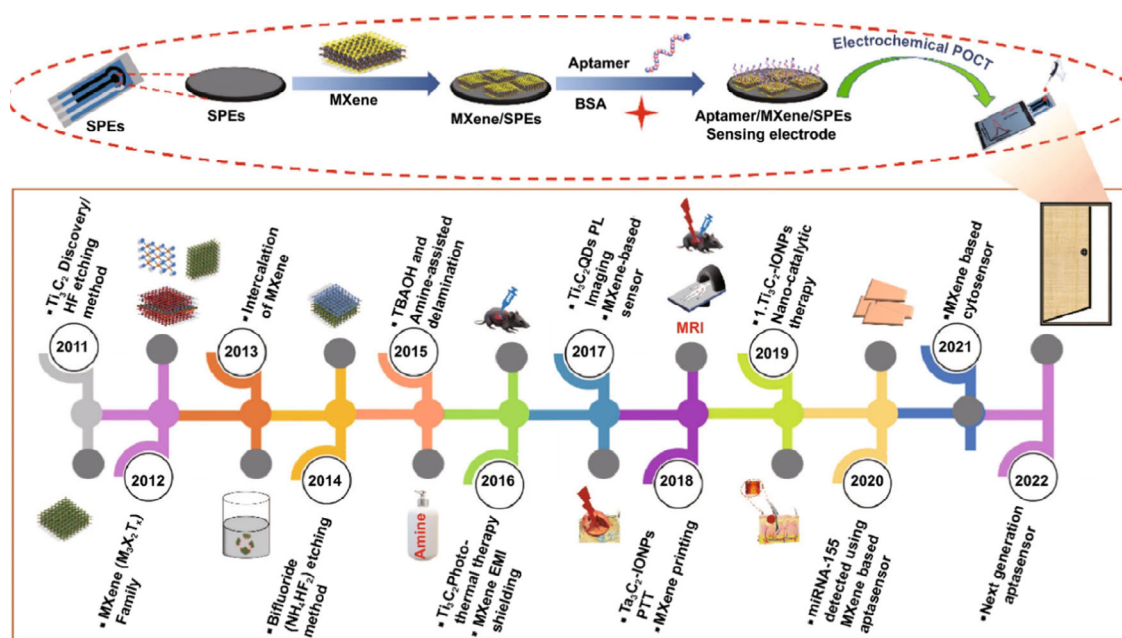


Figure 6. Timeline of MXene for the preparation and implementation into the biomedical area. Reproduced with permission.^[42] Copyright 2022, Springer Nature Switzerland AG.

subsequently investigating the platforms within the tumor. It showed the related IR thermal pictures at tumor areas into groups of BGS + laser and TBGS + laser (Figure 7d). Figure 7e shows that it quickly promoted the exterior

temperature of tumors embedded with 1.0 TBGSs to the equilibrium temperature of 63 °C beneath NIR laser radiation within 2 min. In remarkable distinction, the temperature of tumors rooted with BGSs in the absence of the incorporated Ti_3C_2

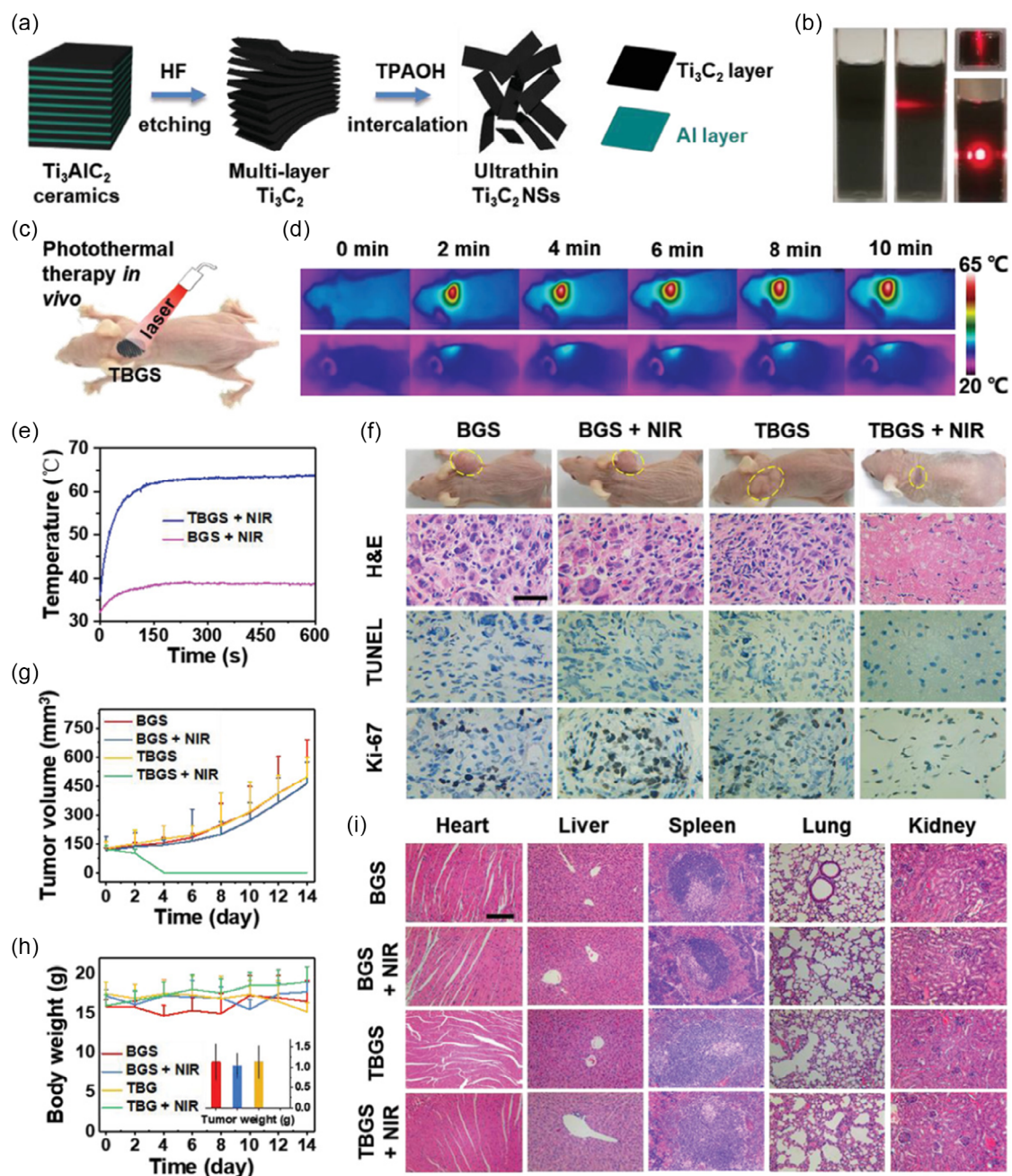


Figure 7. Synthesis and description of 2D Ti_3C_2 MXene NSs. a) Graphic depiction of the construction method of 2D Ti_3C_2 NSs, such as HF etching and TPAOH embolism of the actual bulk Ti_3AlC_2 ceramic. b) Digital pictures of Ti_3C_2 NSs distributed within an aqueous media. In vivo photothermal enactment assessment of TBGSs. c) Graphic description of TBGSs for in vivo photothermal cancer removal. d) The related IR thermal pictures at tumor locations of Saos-2 tumor-carrying mice within groups of BGS + laser and TBGS + laser (base). e) Temperature ridges at tumor spots of Saos-2 tumor-carrying mice within classes of BGS + laser and TBGS + laser. f) Pictures of Saos-2 tumor-carrying mice on 14th day after various therapies, and the tumor tissues impaired through H&E, terminal deoxynucleotidyl transferase-mediated dUTP-biotin nick end labeling (TUNEL) (apoptosis), and Ki-67 (expansion) on one day after multiple remedies (scale bars: 10 μm). g) Time-reliant tumor-transition curves after various therapies. h) Time-dependent body mass arcs of mice after various therapies. Inset: tumor poundage of mice at the 14th day behind various therapies. $N = 5$. i) H&E discoloration of primary organs of Saos-2 tumor-bearing mice upon the 14th day after various therapies (scale bars: 100 μm). Reproduced with permission.^[50] Copyright 2019, John Wiley and Sons.

MXene scarcely grew to $\approx 37^\circ\text{C}$. As indicated from the related tumor pictures (Figure 7f), the tumors in ministered groups (TBGS + NIR) were removed entirely by photonic tumor hyperthermia deprived of reoccurrence. The tumor volumes of the medicinal group illustrated prominent conquest with the whole absolute abolition. In contrast, the tumor volume of the command groups proliferated (Figure 7g). In the meantime, all groups' body weights (Figure 7h) showed no substantial distinction, indicating that either pure BGSs or TBGSs caused no apparent toxicity. After that, it is necessary to demonstrate hybrid platforms' possible critical and enduring poisonousness. Further, the histocompatibility of the compound platforms is considered by H&E staining of the primary organs of mice at the 1st, 14th, and 28th days after photothermal excision (Figure 7i).^[50]

Anchun et al.^[51] focused on ultralong hydroxyapatite nanowires (UHAPNWs) that were fabricated with $\text{Ti}_3\text{C}_2\text{T}_x$ NSs effectively via solution coblending self-decorated process and vacuum-aided percolation. The UHAPNWs/MXene nanomaterial films showed a layer-by-layer loading with ultralong NWs struck, wound, and overlaid homogenously between flakes that are briefly described in Figure 8a. One investigation presented $\text{Ti}_3\text{C}_2\text{T}_x$ NSs within a polylactic acid medium to demonstrate their fantastic possibility for suggested bone rejuvenation in vitro trials.^[52] According to their analysis, it was the first report to include UHAPNWs as support within MXene to improve the mechanical and biological characteristics. Numerous NSs may be combined with ultralong NWs by constructing hydrogen bonds to assemble a more immediate connection between the two inorganic stages (Figure 8b). Accordingly, the UHAPNWs/MXene nanomaterial

membranes have good mechanical features, desirable biocompatibility, and superior osteoinductivity.

In vivo investigations were taken out to demonstrate the osteogenic ability of the UHAPNWs/MXene nanomaterial films. As displayed in Figure 8c, the MXene sheet and its nanomaterial membrane contained equivalent verges with bone tissue. It can observe unique bone construction from the internal perspective of the 3D reconstruction pictures of calvarial bone imperfections. Meanwhile, the superficial view can see the therapeutic procedure's physical combination of the used films. Figure 8d shows a surgical approach to make rat calvarial imperfection standard and cover the bone imperfection with appropriate membranes. The MXene group showed a mass of recently developed bone extending from boundaries and a few bone islands fibbing within the defect zone. It filled imperfections in the UHAPNWs/MXene group with the utmost restored bone. To quantitatively examine the renewed bone tissue, bone volume segment (BV/TV), trabecular width (Tb.Th) and trabecular segment (Tb.Sp) are estimated in Figure 8e.

As a component of the MXene family, the Ti_3C_2 nanofilms with a 2D network have been prepared based on the facile HF-etched approach. This possesses better photothermal alteration activity for NIR-II-persuaded mild hyperthermia and perfect PAI capability. Similarly, the MXene texture was adorned with platinum NPs based on a straightforward and in situ sol-gel chemistry (Figure 9a). Boosted with the ideal activity of $\text{Ti}_3\text{C}_2\text{T}_x$ -Pt-PEG nanomaterials, additionally, the in vitro therapeutic effectiveness utilizing the murine 4T1 breast cancer cells (Figure 9b) is assessed. At an absorption of $200\ \mu\text{g mL}^{-1}$, both delivered lower poisonousness to the normal cells at 12 and

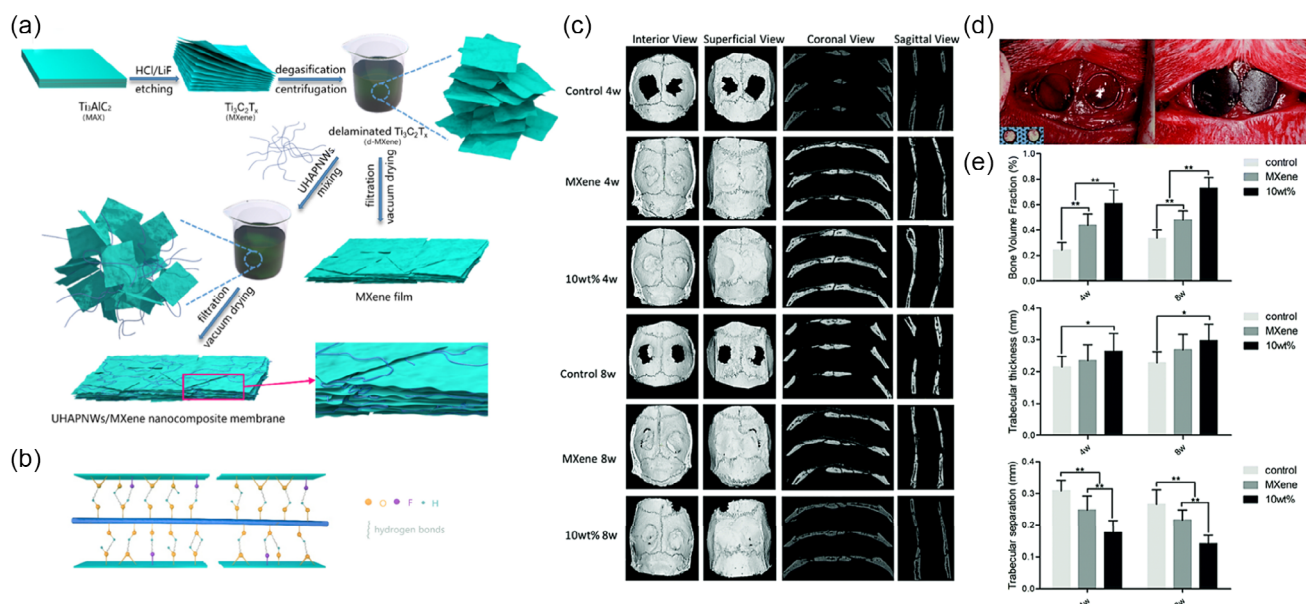


Figure 8. a) Graphic description of the incorporation of the UHAPNWs/MXene nanomaterial film. b) Visual chart of the relations among UHAPNWs and MXene, concerning the hydrogen bonds constructed through completed exterior groups of MXene ($-\text{F}$, $=\text{O}$ or $-\text{OH}$) and hydroxyl in UHAPNWs. Bone revival activity within the managing group, MXene group, and UHAPNWs/MXene group at 4 and 8 weeks after surgery; c) 3D rebuilding pictures of the bone deficiency, as well as interior and external ideas related to micro-computed tomography (CT) pictures such as coronal and sagittal beliefs. d) A surgical procedure to construct a rat calvarial imperfection prototype and protect the bone imperfection with appropriate films. e) Radiographic investigation of bone morphometric constraints, including BV/TV, %, Tb. Th, mm, and Tb. Sp, mm, $*p < 0.05$, $**p < 0.01$ corresponding with distinguished groups. Reproduced with permission.^[51] Copyright 2021, Elsevier Ltd.

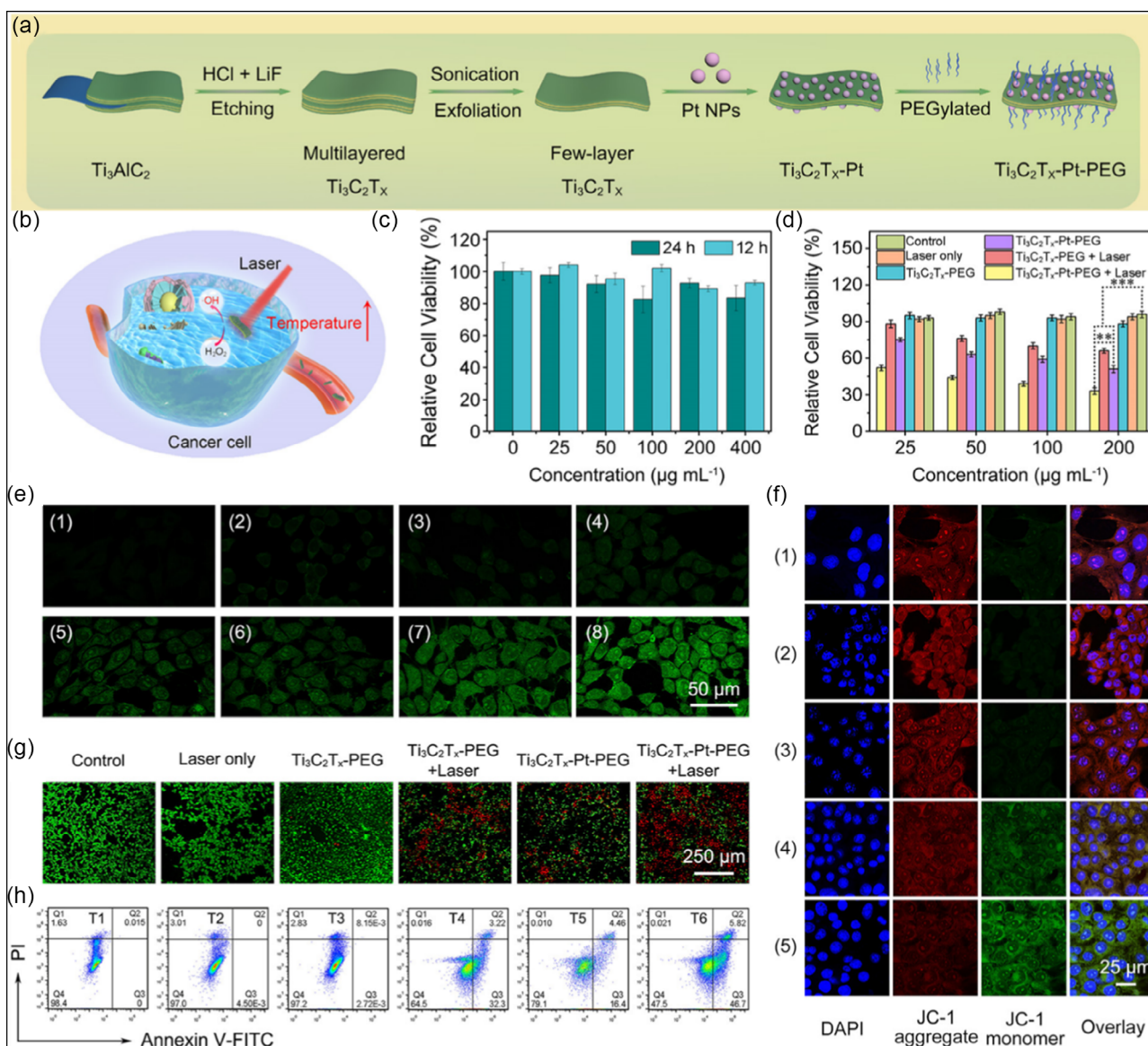


Figure 9. a) Diagram of the artificial process of $\text{Ti}_3\text{C}_2\text{T}_x\text{-Pt-PEG}$. Assessment of photothermal-improved tumor nanocatalytic healing efficacy. b) Graphic design for synergistic treatment upon 4T1 cells, including $\text{Ti}_3\text{C}_2\text{T}_x\text{-Pt-PEG}$. c) Comparative cell feasibilities of L929 cells raised by $\text{Ti}_3\text{C}_2\text{T}_x\text{-PEG}$ and $\text{Ti}_3\text{C}_2\text{T}_x\text{-Pt-PEG}$ at dissimilar absorptions for 12 and 24 h. d) Cytotoxicity outlines of 4T1 cells after existence preserved with diverse designs. Information was accessible as mean \pm SD ($n = 3$). Arithmetic implication is assessed through a two-tailed student's t test, $**p < 0.01$, $***p < 0.001$. e) Confocal laser scanning microscopy (CLSM) pictures of intracellular reactive oxygen species (ROS) equal to 4T1 cells with dissimilar processing. f) JC-1 discoloration of 4T1 cells within diverse groups. g) Calcein-AM/PI discoloration and h) stream cytometry investigation of 4T1 cells nurtured with diverse preparations. Reproduced with permission.^[53] Copyright 2022, American Chemical Society.

24 h, and all the cell feasibilities were beyond 80% (Figure 9c). These outcomes demonstrate that the $\text{Ti}_3\text{C}_2\text{T}_x\text{-Pt-PEG}$ nanomaterials have suitable biocompatibility and would be used for in vivo therapeutic implementations. The cytotoxicity assessment of 4T1 murine breast cancer cells improved with a more elevated absorption of $\text{Ti}_3\text{C}_2\text{T}_x\text{-Pt-PEG}$ NMs in all medicinal classes. As displayed in Figure 9d, the cells feted with a laser exclusively and $\text{Ti}_3\text{C}_2\text{T}_x\text{-PEG}$ at different concentrations demonstrated no apparent differences in their viabilities, comparable with the managing group. The $\cdot\text{OH}$ would respond with the 2,7-dichlorofluorescein

diacetate (DCFH-DA) to assemble 2,7-dichlorofluorescein (DCF) with green fluorescence. As shown in Figure 9e, the 4T1 cells hatched with $\text{Ti}_3\text{C}_2\text{T}_x\text{-Pt-PEG}$ nanomaterials showed better green fluorescence than the other groups (reign, laser solely, and $\text{Ti}_3\text{C}_2\text{T}_x\text{-PEG}$), suggesting that the $\text{Ti}_3\text{C}_2\text{T}_x\text{-Pt-PEG}$ nanomaterials would catalyze intracellular H_2O_2 to outcome $\cdot\text{OH}$. As displayed in Figure 9f, the red fluorescence would be noticed within the reign, 1064 nm laser radiation, and $\text{Ti}_3\text{C}_2\text{T}_x\text{-PEG}$ classes. This could ignore the differences in mitochondrial membrane possibility. The calcein-AM (green) and propidium iodide

(red) double-stain assessment was brought out to additionally assure the adequate removal of $\text{Ti}_3\text{C}_2\text{T}_x\text{-Pt-PEG}$ nanomaterials to 4T1 cells, including laser radiation (Figure 9g). The apoptotic proportion caused through $\text{Ti}_3\text{C}_2\text{T}_x\text{-Pt-PEG}$ beneath 1064 nm radiation, 52.52% (Q2 + Q3), is more significant compared with $\text{Ti}_3\text{C}_2\text{T}_x\text{-Pt-PEG}$ (20.86%) and $\text{Ti}_3\text{C}_2\text{T}_x\text{-PEG}$ under 1064 nm radiation (35.52%) beneath the identical circumstances that comprise early apoptosis and late apoptosis (Figure 9h).^[53]

4.2. MXene-Based Nanomaterials for Cancer Theranostic

In photothermal therapy (PTT)/photodynamic/chemotherapy, the materials capable of absorbing light are supplied to cancer tissues, where the energy of captivated light is transformed into heat to inhibit the growth of tumor cells. Therefore, the material needs to be efficient in converting light into heat energy, highly capable of harvesting the light in the NIR region, biocompatible, and have facile functionalization of the surface.^[54] NIR radiations need efficient light penetration to minimize the tissue's self-heating and maximize the material's photothermal conversion activity.^[55] MXene-based NMs possess the characteristics mentioned earlier and are extensively considered efficient materials in cancer theranostic applications. Cancer ablation of MXene-based NMs via phototherapy utilizing NIR radiations is a technique where tumor ablation is carried out by exploiting the local heating effect with a weakly vascularized microenvironment.^[8b]

For PTT, MXene QDs consisting of Ti_3C_2 and Ti_2C have been designed as a safe, facile, and useful fluorine-free biocompatible agent and MXene QDs exhibit a high extermination constant of $52.8 \text{ Lg}^{-1} \text{ cm}^{-1}$ and photothermal translation proficiency of 52.2% at 808 nm. Further, they are biocompatible without considerable toxicity in vivo and in vitro.^[56] Ti_3C_2 nanosheets with nearly 100 nm pore size are also used for cancer therapy. These nanosheets are prepared by supplying additional Al (III) to avoid loss of Al and display a noteworthy mass extermination constant of $28.6 \text{ Lg}^{-1} \text{ cm}^{-1}$, photothermal translation efficacy (58.3%), and efficient singlet-oxygen production at 808 nm laser irradiation.^[26] These multifunctional nanoplateforms were fabricated via layer-by-layer surface alteration with hyaluronic acid and doxorubicin (DOX), as shown in Figure 10a. They showed improved tumor explicit accretion, better biocompatibility, and stimuli-receptive drug release performance, and effectively hindered and killed carcinogenic cells and tumor tissues by PTT/photodynamic/chemosynergistic therapy. MXene- $\text{Ti}_3\text{C}_2\text{T}_x$ QDs synthesized using the microexplosion method demonstrated killing and obstructive impacts on cancer cells and outstanding biocompatibility. Furthermore, it could reach the rate of suppressed synthesized material on heterograft tumor models at 91.9% without any detrimental effects and damage to normal tissues.

As demonstrated in Figure 10b,c, the temperature of $\text{Ti}_3\text{C}_2\text{-DOX}$ -amassed tumor increased from 34 to 53.1 °C in

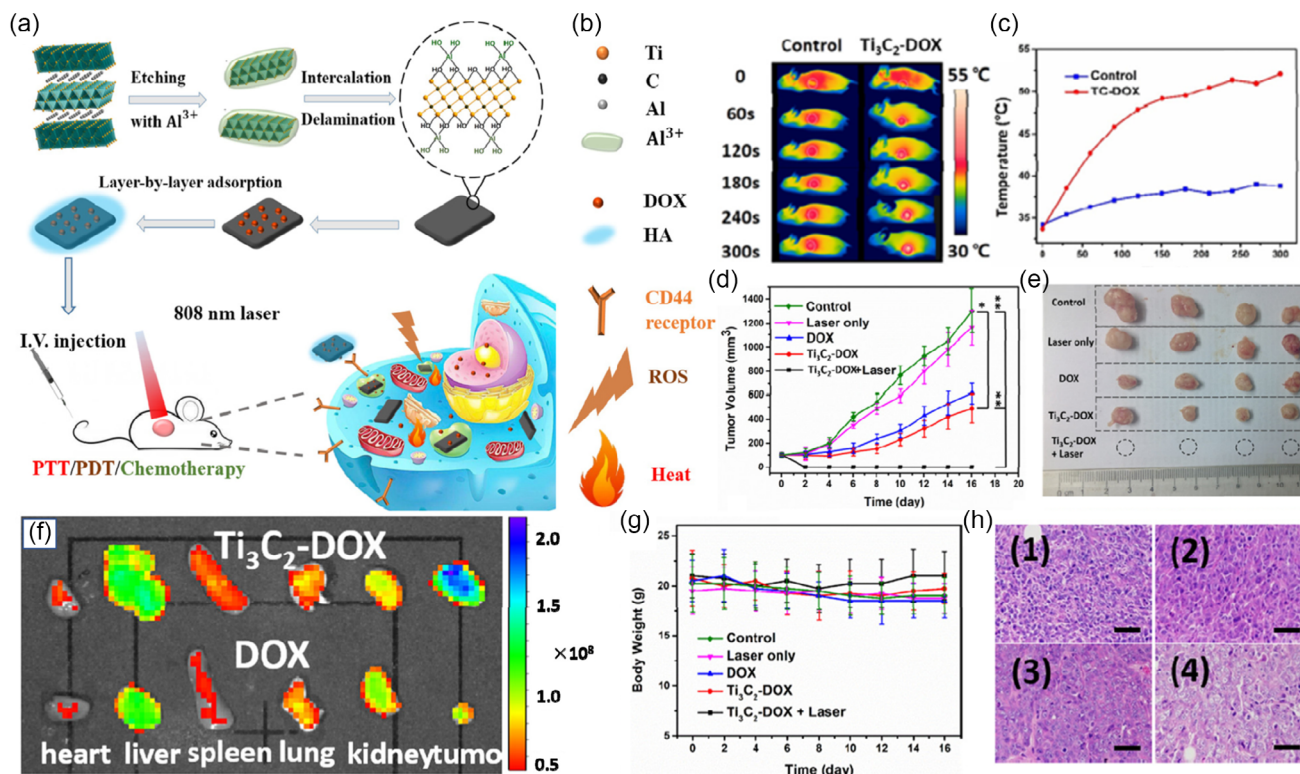


Figure 10. a) Schematic diagram showing the fabrication of Ti_3C_2 MXene nanoplateforms for potential PTT/photodynamic therapy (PDT) or chemotherapy of tumors. b) The IR thermal pictures of rats 6 h postinjection of PBS or $\text{Ti}_3\text{C}_2\text{-DOX}$ below various radiation times and c) temperature shape of tumor. d) Tumor elaboration curves during therapy. e) Digital pictures of tumors after therapy. f) Ex vivo fluorescence pictures of tumor and prominent organ tissues of DOX or $\text{Ti}_3\text{C}_2\text{-DOX}$ -insinuated mice. g) Body weight transition curves of naked mice during therapy. h) Histologic microscopy pictures of tumors after remedies: (1) reign, (2) laser solely, (3) DOX, and (4) $\text{Ti}_3\text{C}_2\text{-DOX}$. Reproduced with permission.^[26] Copyright 2017, American Chemical Society.

5 min, adequate for tumor removal. At the same time, the phosphate buffer saline (PBS) insinuated that mice solely revealed a small temperature growth. Therapy with complimentary DOX or Ti_3C_2 -DOX in the absence of laser radiation only partly impeded tumor development. Comparatively, it eliminates synergetic photodynamic PTT/chemotherapy of Ti_3C_2 -DOX activated through laser radiation tumor without reoccurrence (Figure 10d,e). Figure 10f shows ex vivo fluorescence pictures of tumor and primary organ tissues of DOX or Ti_3C_2 -DOX-insinuated mice. Over 16 d of therapy, excluding the free DOX processing group with a negligible weight loss, the body poundage of all mice groups stayed constant (Figure 10g). All rats of all groups prevailed after 16 d of therapy. After synergistic treatment, we examined the tumor and primary organ tissues. For histopathological investigation, the tissue portions were shaded with H&E (Figure 10h).

The authors found that Ti^{3+} of MXene- $Ti_3C_2T_x$ QDs reached the tumor microenvironment with hydrogen peroxide and effectively produced enormously poisonous hydroxyl radicals, which surge tumor microvascular penetrability for synergistic annihilation of cancer cells.^[57] Heterostructure Ti_3C_2 -based MXene NWs (Ti_3C_2 -Co NWs) were synthesized for supportive anticancer with magnetic-controlling potential, chemo-PTT having dual stimuli-responsive drug release.^[58] This nanocarrier heterojunction established outstanding photothermal translation efficiency within 808 nm laser radiation and a high drug packing capacity of 225.05%. It could generate the discharge behavior of DOX via NIR radiation within the acidic medium (pH ranges from 4 to 6). Compared with individual chemotherapy or PTT, it had

significant lethality for cancer cells. The synthesis process of Ti_3C_2 -Co nanowires, along with stimuli-responses to drug discharge, is showcased in Figure 11a,b. Figure 11c illustrates the Ti_3C_2 -CoNW nanocarrier heterojunction effectively entering the cancer cells through endocytosis and then killing the cancer cells on NIR radiation via chemophotothermal treatment. As per the correlated benchmark, the cytotoxicity groups of these models were grade 1 that can be used for biomedical substances.

Hence, the accumulation of magnetic fields did not affect cytotoxicity. As displayed in Figure 11d, 92, 73, 74, and 67% of 4T1 cells are possible for 24 h after being preserved with DOX@ Ti_3C_2 -CoNWs at different absorptions of 25, 50, 100, and 200 $\mu\text{g mL}^{-1}$ concurrently. NIR radiation was used for 20 min after a gestation of 4T1 cells with free DOX, Ti_3C_2 -CoNWs, and DOX@ Ti_3C_2 -CoNWs for 24 h, correspondingly. As displayed in Figure 11e, no substantial difference in the cell feasibility after NIR radiation exists for the control group, showing that the NIR laser independently does not wind the cells. At the same time, the calcein-AM hydrolyzes to green fluorescent calcein within living cells, and propidium iodide (PI) stains the DNA of cells killed as red. As displayed in Figure 11f, DOX@ Ti_3C_2 -CoNWs lead to a comparable cell-killing consequence to the free DOX assembly.

Dia et al.^[22b] constructed MnO_x/Ti_3C_2 initiated via a simple redox reaction for the facile growth of tiny MnO_x nanosheets on the superficial Ti_3C_2 . The prepared composite can be considered a versatile cancer theranostic agent for potential magnetic resonance (MR) and photoacoustic dual-modality

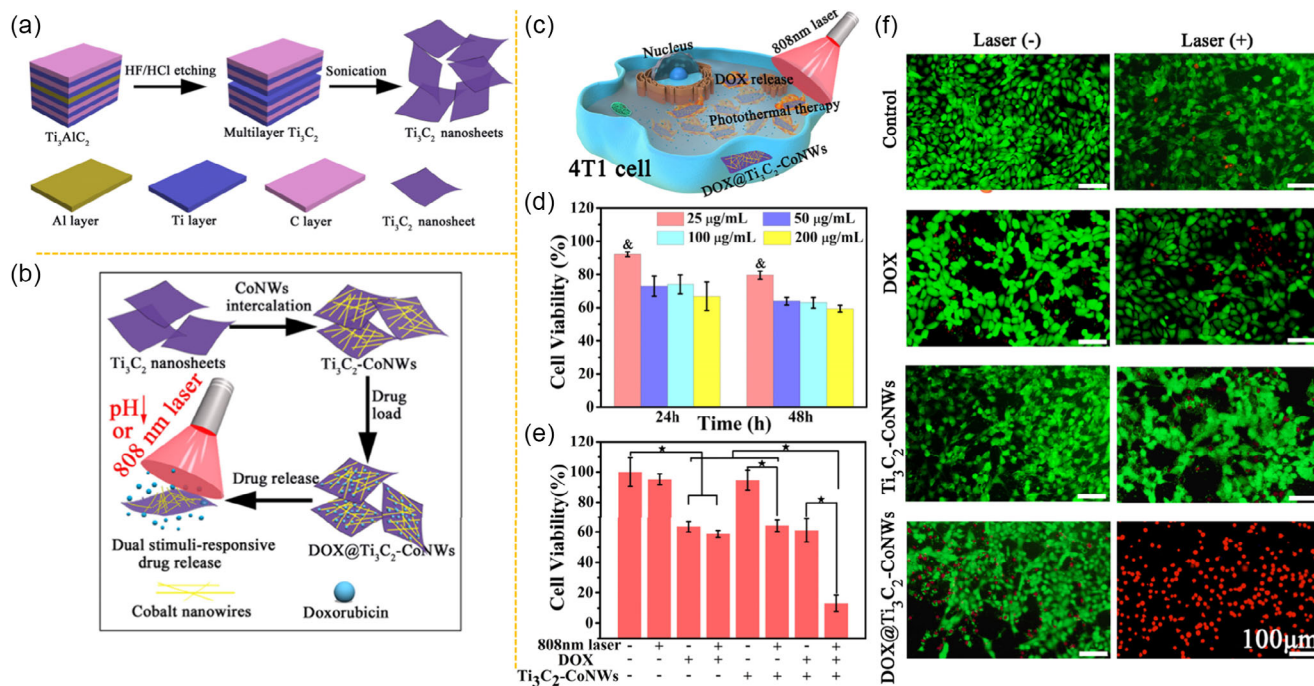


Figure 11. a,b) Fabrication of Ti_3C_2 NSs and their amalgamation with Co NWs for dual stimuli-receptive DOX drug discharge. c) Graphic description of Ti_3C_2 -CoNWs nanocarrier heterojunction for chemophotothermal synergetic treatment against cancer cells. d) Cell feasibility of 4T1 cells after being preserved with DOX@ Ti_3C_2 -CoNWs at distinct absorptions for 24 and 48 h ($n = 3$). Numerical examination was completed through the student's *t*-test ($p < 0.05$). e) Cell feasibilities of 4T1 cells after dissimilar therapies with an absorption of 50 $\mu\text{g/mL}$ of all tasters ($n = 3$). Numerical investigation was completed through the student's *t*-test ($*p < 0.05$). f) Fluorescence pictures of 4T1 cells after being treated by uncontaminated DOX, Ti_3C_2 , Ti_3C_2 -CoNWs, and DOX@ Ti_3C_2 -CoNWs. Reproduced with permission.^[58] Copyright 2020, Elsevier Ltd.

imaging-shown PTT. The role of the decoration of the MnO_x constituent on MnO_x/Ti_3C_2 was explained by the authors that it provides exclusive tumor microenvironment-receptive T1-biased MR imaging of tumors. The enhanced photothermal translation proficiency provides attractive contrast-enhanced photoacoustic imaging to MnO_x/Ti_3C_2 , suppresses tumor growth cells, and effectively ablates tumor. Table 1 displays the synthesis methods and different functions of MXene-based NMs.

4.3. MXene-Based NMs for Antiviral and Immunomodulatory Properties against SARS-CoV-2

From the starting of the coronavirus disease 2019 (COVID-19) pandemic, induced through the novel SARS-CoV-2, researchers with various experiences have collaborated to handle these problems.^[70] Additionally, extensive preclinical and clinical tests have been carried out to configure drugs and vaccines. Various analysis measures are being executed to execute better viral inactivation techniques beyond the patients, for example, developing self-disinfecting exteriors or personal protective equipment (PPE).^[71]

Numerous studies emphasized how nanotechnology and 2D NMs may suggest new strategies to manage the COVID-19 pandemic and communicable diseases in general, including near-days pandemics.^[72] 2D NMs have been studied for various biomedical utilizations, such as cancer theranostics, biosensors, and antimicrobial scaffolds.^[73]

Unal et al.^[74] followed material preparation and characterization. They performed a thorough antiviral and deep-immune profiling investigation (Figure 12a). To quantify viral reproduction numeral, culture supernatants after analyzing viral infection through qRT-PCR are shown. As shown in Figure 12b, while significantly reduced infected cells with SARS-CoV-2 within $Ti_3C_2T_x$, the viral copy numeral of GR clade on each dilution experimented, as corresponded to the cells feted with the virus solitary; additionally, 99% inhibition was acquired already on 1:3,125 dilution. Another side observed no substantial consequence for the additional genotypes (Figure 12c–e). To confirm the inhibition spectacle honored in the GR clade, they evaluated the feasibility of Vero E6 cells following disease. Remarkably enhanced feasibility of Vero E6 cells with the material corresponded to the cells feasted with the virus sole (Figure 12f).

Table 1. Preparation methods and different functions of MXene-based NMs.

MXene-based NMs	Preparation method	Region	Wavelength [nm]	Power density [$W\ cm^{-2}$]	Photothermal conversion efficiency [%]	Extinction coefficient [$Lg^{-1}\ cm^{-1}$]	Mode of therapy	References
Ti_3C_2 -IONPs	In situ	NIR-I	808	1.5	48.6	7.9	MRI + PTT	[59]
$GdW_{10}@Ti_3C_2$	Top-down exfoliation	NIR-I	808	1.5	21.9	22.5	MRI/CT + PTT	[60]
Ti_3C_2 QDs	Sonication technique	NIR-I	808	1.0	52.2	52.8	PTT	[56]
Ti_3C_2 nanosheets	Modified chemical exfoliation method	NIR-I	808	1.5	30.6	25.2	PTT	[9b]
MnO_x/Ta_4C_3	In situ facile redox reaction	NIR-I	808	1.5 and 2.0	34.9	8.67	PTT + CT + PA + MRI	[61]
Ti_2C -PEG	–	NIR-I	808	–	87.1	7.39	PTT	[22c]
NPD@M	–	NIR-I	1064	0.5	51	–	PTT	[62]
		NIR-II	808					
Ti_3C_2 MXene modified with GOX, sodium ascorbate, and dopamine	HF etching	NIR-I	808	2	45.1	–	PTT	[63]
Ti_3C_2 -PVP@DOXjade	HF etching	NIR-I	808	1 and 1.5	40	–	Chemo-PTT	[64]
Ti_3C_2 -Co	Sonication	NIR-I	808	1.5	34.42	–	PTT	[58]
$Ti_3C_2T_x$ -Pt-PEG	–	NIR-II	1064	0.75	31.78	4.81	PTT	[53]
2D-Nb ₂ C MXene	Sol-gel technique	NIR-II	1064	1.5	28.6	–	PTT and chemotherapy	[65]
$Ti_3C_2@Au$	Seed growth method	NIR-I	808	0.75	34.3	–	PA + CT + PTT	[66]
		NIR-II	1064		39.6			
Titanium nitride QDs	Delamination process	NIR-I	808	–	48.62	–	PA + PTT	[67]
		NIR-II	1064		45.51			
Niobium carbide- MXene	Modified chemical exfoliation process	NIR-I	808	–	36.4	37.6		[68]
		NIR-II	1064		45.65	35.4		
Ta_4C_3 -MXene	HF etching	NIR-I	808	1.5	32.5	–	PTT + MR	[9d]
Mo_2C -MXene/polyvinyl alcohol	Acid etching	NIR-I	808	1.0	24.5	18.0	PTT	[69]
		NIR-II	1064		43.3	12.3		

MRI: Magnetic resonance imaging; CT: Computed tomography; PA: Photoacoustic imaging; IONPs: Iron-oxide NPs; NPD@M: Nb₂C plasmon, Pt nanozymes, DOX@MXene; GOX: Glucose oxidase.

Furthermore, no toxicity was marked while the cells were preserved with only the NM (Figure 12g).

4.4. Biosafety of MXenes-Based NMs for Biomedical Application

Biocompatibility and toxicity are essential factors that should be systematically examined for thriving clinical translation of MXene-based NMs with the biomedical application.^[37a,75] The possible cytotoxic consequences of these NMs upon human cells are mainly related to their physicochemical effects, cellular exchanges, and assemblies within the targeted organs/tissues.^[76] Therefore, these NMs' cellular/molecular relations and toxicological characteristics should be intensely studied, including penetration/branch, endocytosis, potential DNA harms, inflammatory reactions, apoptosis, etc.^[16,65] In a few investigations, physical harm, changes within the subcellular internalization tools, and

the oxidative stress induced by the generation of dynamic, responsive oxygen species have been reported as potential poisonous tools of MXene-based NMs.^[77] It seems that complete and detailed in vitro/in vivo investigations are yet needed to illustrate toxicity mechanisms and long-term biosafety inspections. Few experiments showed that MXenes could have deadly consequences on zebrafish embryo standards (an in vivo analysis).^[78]

In this regard, Nasrallah et al.^[79] developed and executed a method to assess the toxicological impact of $Ti_3C_2T_x$ utilizing a zebrafish model to investigate possible negative consequences of $Ti_3C_2T_x$ in vivo and especially on marine biota. The investigation focused on the ecotoxicological examination of $Ti_3C_2T_x$, which can create a scaffold for prospective toxicological analyses on other practical representatives.

In addition, these materials can enhance biocompatibility, pharmacokinetics, and biodegradability by hybridizing eco-friendly preparation methods with natural polymers and exterior

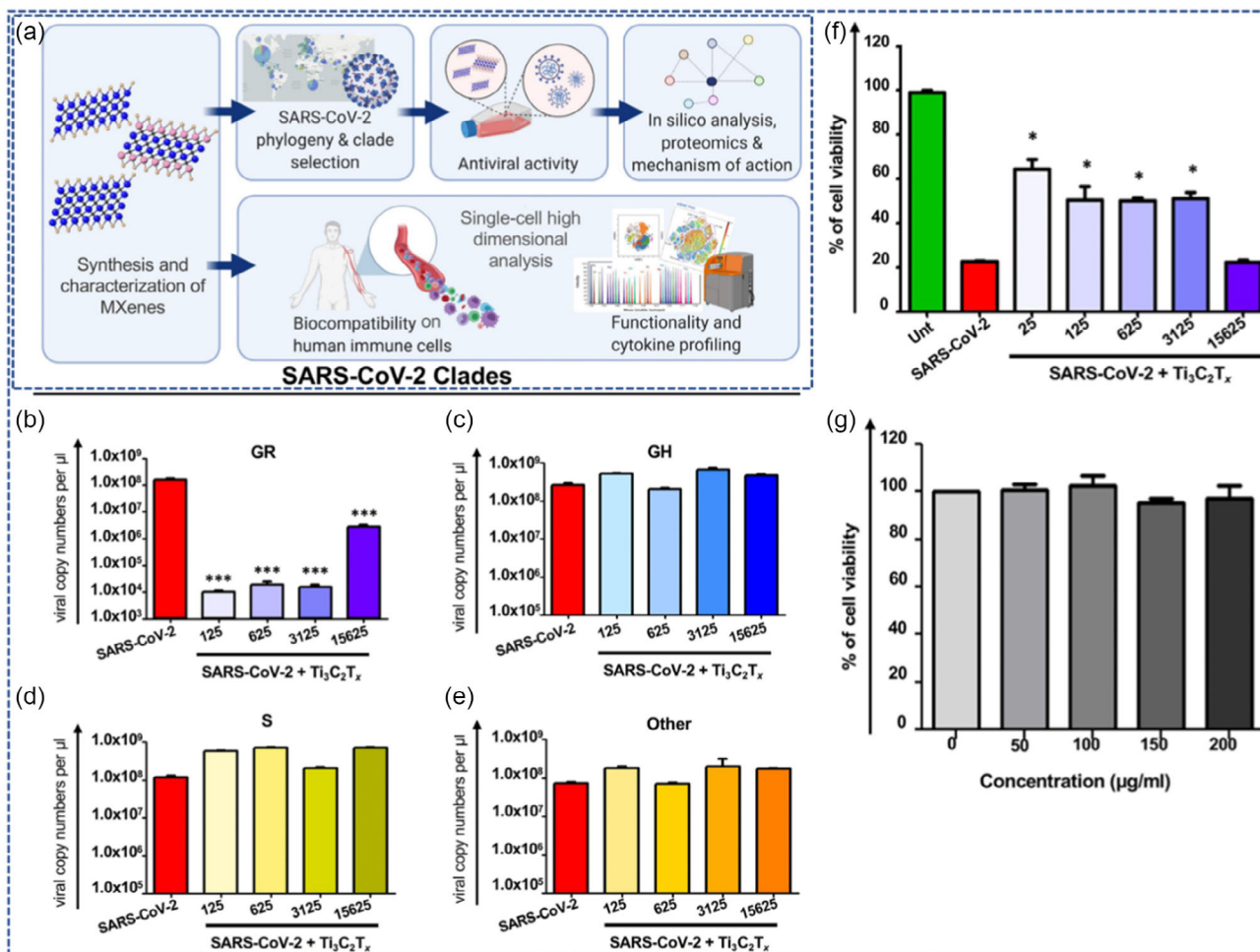


Figure 12. Analysis technique and material description. a) Outline of the investigation procedure. Antiviral performance of $Ti_3C_2T_x$ upon the disease of chosen genotypes and transformations of SARS-CoV-2. Analyzed infected Vero E6 cells with SARS-CoV-2 with $Ti_3C_2T_x$ at different dilutions and after 48 h, viral compositions within cell culture supernatant through qRT-PCR. The four distinct viral genotypes were chosen and illustrated: b) GR, c) GH, d) S, and e) other. f) Assessed infected Vero E6 cells with SARS-CoV-2 with $Ti_3C_2T_x$ at various dilutions, and after 48 h, the feasibility of cells and rate of viability are connived. g) It determined and assessed the toxicity of $Ti_3C_2T_x$ within Vero E6 cells following material orientation around 4 h. Rate of viability via LDH assay. Statistical distinctions: * $p < 0.05$; *** $p < 0.001$ resembled to just virus group. Three specimen models for every sampling group were analyzed. Reproduced with permission.^[74] Copyright 2021, Elsevier Ltd.

functionalization/transformation with bioactive/biocompatible agents.^[22a,22b,80] For example, Pu et al.^[81] used an ecofriendly approach to use chitosan with renewability and nontoxicity benefits for manufacturing nitrogen-doped MXene-based NMs. These factors mentioned above may also enhance their targeting characteristics (selectivity and particularity) and decrease possible off-target consequences and undesired circumstances like accretion or assemblage, which may restrict their future biomedical and clinical potentials and facilitate their functionality.^[37a,82]

Furthermore, studies of hematology parameters, biochemical blood directories, and histopathological analysis of rats for 28 days showed that circulatory Nb₂C-PVP did not cause many rashes, disease, and renal and hepatic poisonousness in vivo.^[28] Additionally, the establishment of an MXene sheet within intravenous tissues into rats resulted in mild rash and granulation in the tissue covering the smashed MXenes and multiple fibroblasts and capillary containers. Macrophages were connected to MXenes, while apparent inflammatory cell infiltration and necrosis were not followed. MXenes were captivated and biodegraded through phagocytosis in vivo.^[83] MXene films cause oxidative pressure that is poisonous to cancer cells but has excessively low-sensitive cytotoxicity and results in mild inflammatory reactions from normal cells and tissues. Within the secure amount range, MXenes are approvingly biocompatible with an innocuous biodegradation shape both in vitro and in vivo, representing the basis for designing bioapplications. Keeping a safe dosage and optimal activity could be a significant obstacle to advancing the biomedical consequence of MXenes.

4.5. Other Biomedical Applications of MXene-Based NMs

Figure 13 shows the other biomedical applications of MXene-based NMs in different fields.

4.5.1. Biosensors

The discriminating and responsive recognition of particular substances in the living being's biosensors are utilized. Biosensors

comprise mainly three parts, named as 1) a sensing element for the identification of the corresponding analyte, 2) a transducer for transforming biochemical signals into electrical or optical signals, and 3) a data interpretation unit. MXene-based nanomaterials are suitable for biosensors due to good hydrophilicity, high surface area, high conductivity, outstanding electrical and optical characteristics, and good biocompatibility and nontoxicity.^[84]

H₂O₂ is active oxygen, the main medium for phagocytic cells and the byproduct of several oxidases in the human body. Nevertheless, extreme dynamic oxygen generation under pathological circumstances severely affects the cell membrane and can even damage protein, cells, etc., in organisms. Thus, the potential determination of H₂O₂ at early stages is crucial for diagnosing these illnesses. To effectively detect H₂O₂, Nagarajan et al.^[85] fabricated Ti₃C₂T_x-Fe₂O₃ composite via ultrasonication. This composite has a surface area of 0.18 cm² and has high selectivity and sensitivity of 0.32 μA nM⁻¹ cm² with a linear array of recognition from 10 to 1000 nM. 7.46 was the limit of detection for the as-prepared composite.

Another researcher^[86] synthesized MXene/La³⁺-doped ZnO/hemoglobin (Hb) NC for voltammetric detection of H₂O₂ by the hydrothermal method. At pH 7.0, the authors observed a linear range of 0.2–400.0 μM with a lower recognition limit of 0.08 μM and a correlation coefficient of 0.9995. The recovery rate was found to be nearly 100%. Furthermore, Flavin adenine dinucleotide/Ti₃C₂T_x were prepared for an electrocatalytic diagnosis of H₂O₂ in a neutral medium and showed a linear range of detection for H₂O₂ from 5 nM to 2 μM and had a surface area of 0.13 cm² with a limit of detection of 0.7 nM. The composite maintained a selectivity of ≈98% and demonstrated high sensitivity of 0.125 μA nM cm⁻² compared with nonenzymatic sensors.^[87] To monitor H₂O₂ in biological samples, Ti₃C₂T_x/chitosan/Prussian blue-based sensor was developed, which shows good selectivity with a lower limit of detection of 4 nM with a broad linear range between 50 nM and 667 μM and showed 100.3% recovery rate.^[88]

Au/Ti₃C₂ NC has been synthesized for the sensitive detection of glucose. In this biosensor, glucose oxidase was immobilized to

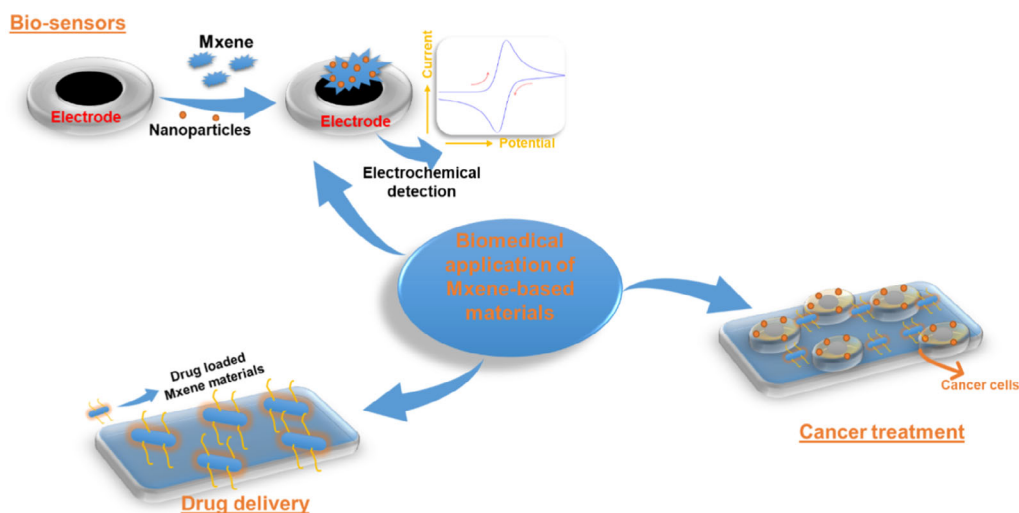


Figure 13. The biomedical applications of MXene-based NMs.

a suitable electrochemical transducer, which was further functionalized with Au. Glucose was oxidized to gluconolactone and H_2O_2 by glucose oxidase, while the electron transfer process was enhanced between glucose oxidase and Au-coated glassy carbon electrode (GCE) by Au. The authors observed that the prepared NC exhibits a high sensitivity of $4.2 \mu A mM^{-1} cm^{-2}$ and a wide linear range (0.1–18 mM) with a lower limit of detection ($5.9 \mu M$) and outstanding reproducibility.^[89]

Figure 14a illustrates the facile appliance incorporation procedure. An explicit slice network is kept within the TEM picture (Figure 14b). The consistency of the fragment is around 4.2 nm, conferring the atomic force microscopy (AFM) measure (Figure 14c) that is in better accordance with prior information. By approximating the SEM pictures of the tissue composition, the homogenous layer of MXene upon degradable porous tissue paper may be followed in Figure 14d,e, which illustrates SEM pictures of the MXene/tissue paper. Figure 14f,g shows the optical images of the accumulated appliance with outstanding elasticity.

The specimens were connected to the skin using medicinal adhesive tape for all human body interchanges. The MXene/tissue paper-based strain sensor was fastened to arm muscles. It was utilized to catch the circular muscle compaction by reversibly causing a fist (Figure 14h). It is precious for physical activity and even possibly for healing muscle deterioration. After constructing a fist, the current gesture improved along with the condensation of the sensor. Figure 14i displays that a sensor was attached to a nerve for real-time monitoring of constriction, one of the physical gestures of humans.

Moreover, the pressure device involved a collar for real-time recognition of consumption and communication, showing wide-ranging current peaks beneath the outside pressure (Figure 14j). The MXene/tissue paper-based pressure sensor would be utilized for the convenient intensive care of the physical strength of the wrist pulse for possible infection analysis (Figure 14k,l). As demonstrated in Figure 14m, a sugar pellet (2.3 mg) with a base area of $1.5 mm \times 1.5 mm$ was incorporated into the exterior of the pressure sensor to get practical recognition boundary, which was initiated to be 10.2 Pa. Knocking on the pressure sensor at a relevant feature frequency would lead to early-phase Parkinson's disease (PDs) with inert temblors (Figure 14n). The magnified views of the emulated colliding upon the pressure sensor with the stationary temblor frequency at 5 Hz are shown in Figure 14o, indicating its possible application for early-stage PD healthcare projection. As demonstrated in Figure 14p, Morse code was introduced with the adjoining pressure sensor, exhibiting the result of the sensing arcs of the current reactions with five related types, for example, "MXene".

Tuning the surface ends of MXenes may also be helpful for different sensing implementations. MXene-based gas sensors use the transitions within MXene conduction during gas-particle extension. Founded on DFT computations, Ti_2CT_x single layer with oxygen ends was incredibly particular for ammonia (NH_3) comparative to additional gas molecules. The outcomes demonstrated that NH_3 molecules would be extremely adsorbed upon the oxygen-ends M_2CT_x family of MXenes, directed to charge transference. Succeeding NH_3 desorption may alter the system's charge state by tuning the electrons insinuated within M_2CT_x .

MXene was also employed for sensitively detecting phenols based upon the direct electron transfer among tyrosinase and MXene-modified electrode via a surface-controlled electrochemical method.^[36] Alkali-inserted $Ti_3C_2T_x$ MXene was employed to detect trail heavy metal ions. The alk- $Ti_3C_2T_x$ -incorporated GCE suggestively improved the electrochemical reaction compared to the new $Ti_3C_2T_x$ -doped electrode. Beneath the optimum circumstances, the extended sensor demonstrated excellent sharpness and good unbenet correlations, with a detection boundary of 0.041, 0.098, 0.032, and $0.130 \mu M$ for Pb^{2+} , Cd^{2+} , Cu^{2+} , and Hg^{2+} , correspondingly (Figure 15a–d).^[91] Another $Ti_3C_2T_x$ -incorporated GCE has been utilized for the electrocatalytic sensing of BrO_3^- into water with a reasonable recognition limitation.^[92]

Surface-Enhanced Raman Spectroscopy Substrates for Biomedical Applications: Cancer has evolved into a significant assassin endangering human health in today's civilization. SERS can deliver a challenging option for sensitively detecting cancer-related miRNAs. Thus, one of the most critical investigations in SERS was examining novel and high-performance nonmetallic supports. Recently, it proved that 2D substances like graphene have SERS performance. Its wide assortment and chemical arrangement produced the great interest of investigators.^[93] For example, Ti_3C_2 was connected with analyte molecules through hydrogen bonds, coordination bonds, and van der Waals interaction to acquire remarkable and steady Raman feature peaks for exact quantitative recognition used for Ochratoxin A implementation.^[94]

Liu et al.^[95] proposed a synergistic calibrated SERS method based upon MXene/molybdenum disulfide (MoS_2)@Au NPs (MMA) with the controllable surface recommended for the ultrasensitive recognition of miRNA-182 via determining the intermediate intensity of its three own expected Raman peaks (at 382 and $402 cm^{-1}$ corresponding to MoS_2 and $611 cm^{-1}$ equivalent to MXene) as a model rather than other beacon molecules. The recognition of miRNA-182 based on MMA's synergistic calibrated SERS technique shows a sensitive detection scope from 10^{-9} to $10^{-17} m$ (Figure 16a). Comparatively articulating, for easy support, the restricted range from 10^{-12} to $10^{-16} m$ toward MoS_2 @AuNPs and from 10^{-12} to $10^{-15} m$ for MXene@AuNPs indicates that MMA has tremendous benefits within ultrasensitive recognition that can be due to the fact that accessible supports may not absorb sufficiently AuNPs to build compelling local surface plasmon resonance (Figure 16b,c). As miRNA-182 concentration declines, the start of hairpin investigation DNA with the stem-loop design reduces, resulting in the intensity growth of the peak at $1362 cm^{-1}$ for MMA, while the peak intensities at 382, 402, and $611 cm^{-1}$ are unchanged. The change of I_{rf} is considerably less compared with each peak (Figure 16d). Likewise, the peak potency performance is also reflected within MoS_2 @AuNPs and MXene@AuNPs. However, the oscillations of single and double peaks for specific supports utilized for calibration are better enunciated compared with the same heights of MMA, suggesting that the self-standard calibration of MMA is more durable and precise (Figure 16e,f). The linear integrity of fit of the synergistic calibrated system, R^2 , is as high as 0.9995, which is relatively more elevated than that of the single- or double-peak calibrated point (Figure 16g). Although the linear recognition range of specific supports for miRNA-182 is from 10^{-12} to $10^{-16} m$, and its recognition

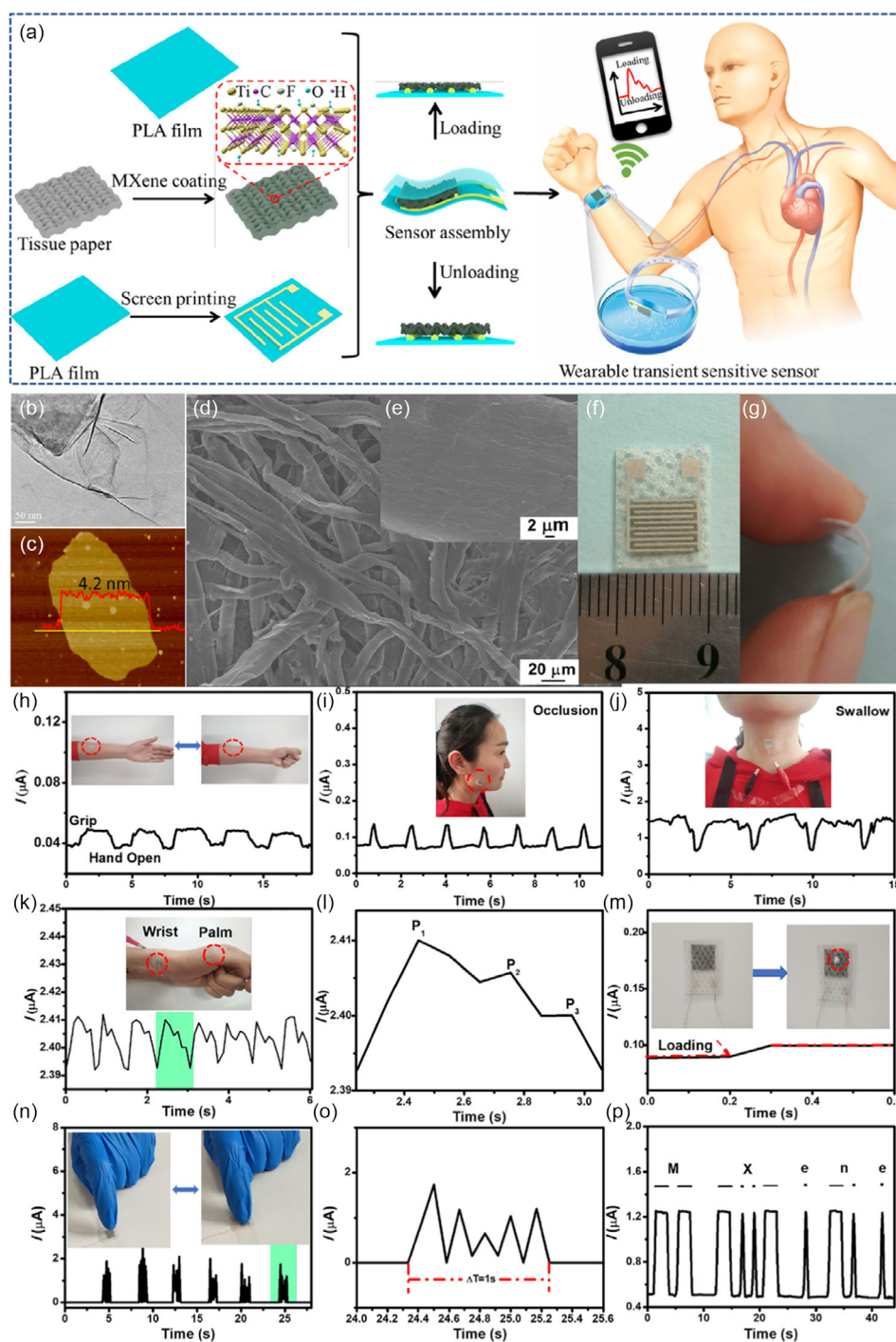


Figure 14. a) Graphic description of the fabrication process of stretchy wear fleeting pressure detectors by MXene NSs. b) TEM picture of the MXene NSs. c) AFM picture of MXene nanofilms dropped upon a mica sheet. d) SEM picture of MXene/tissue paper. e) The widened SEM picture of an MXene/tissue paper fiber. f, g) Photos of the stretchy wear fleeting pressure sensor. h) The sensing arrangement of the pressure detector is connected to the arm strength for dependable recognition of circular muscle compaction resulting from reversibly creating a fist. Inset: Illustration of the sensor fastened to the arm muscle during convertibly creating a bunch. i) Sensing act of the pressure sensor ascended on the nerve for real-time monitoring of constriction. Inset: Picture of the sensor adhered to the cheek. j) The sensing act of the pressure sensor attached to a human gorge for the punctual sensing of consumption. Inset shows a picture of the sensor connected to a human throat. k) The sensing arrangement of the pressure sensor is covered upon the wrist for perceiving wrist pulsing. Inset: Picture of the sensor adhered to the wrist and palm. l) The magnified waveform of blood pulsing. m) The current reaction of the sensor on doping a sugar grain (2.3 mg). Inset shows a picture of a sugar grain (2.3 mg) incorporated into the sensor. n) The sensing recital of the sensor imitation the colliding of early-phase PDs containing a static temblor frequency of 5 Hz. Inset: The emulated colliding of the sensor. o) The magnified sensing activity of imitative knocking. p) The sensing activity of Morse code for “MXene” delivered through adjoining the sensors. Reproduced with permission.^[90] Copyright 2019, American Chemical Society.

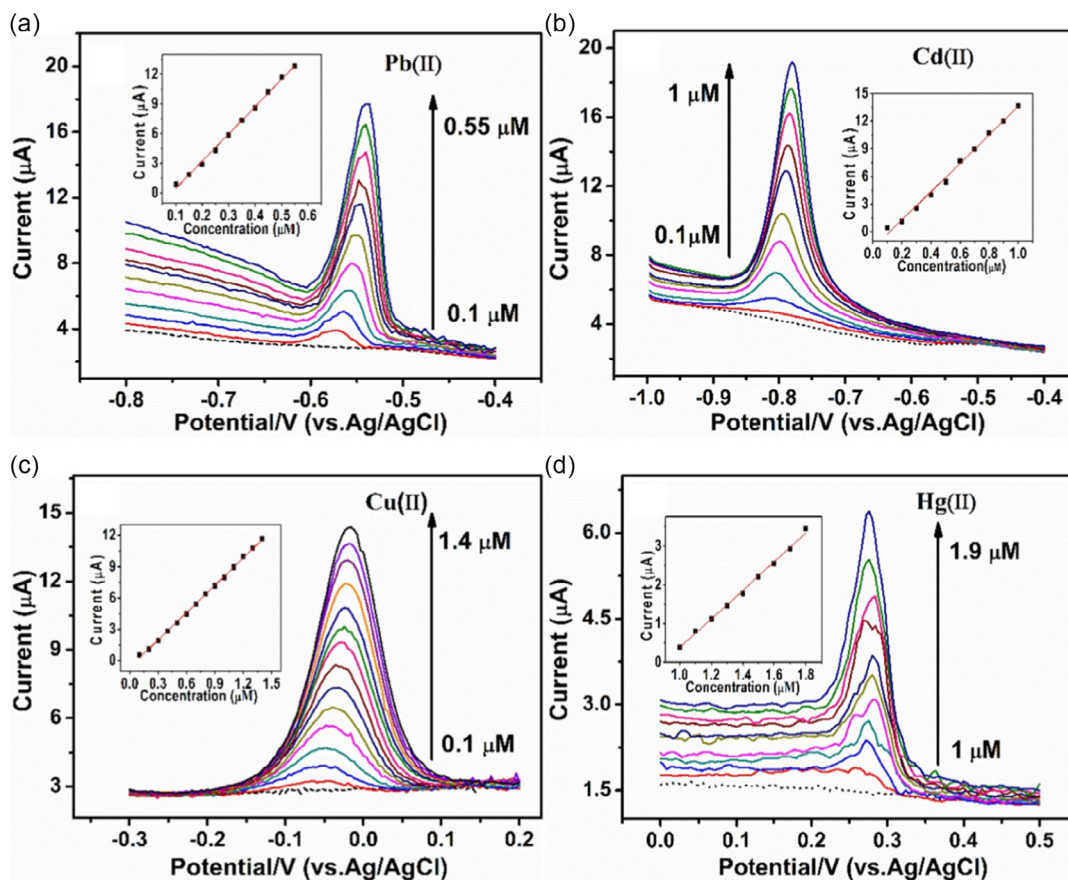


Figure 15. Squarewave voltammetry (SWV) reaction of the alk- $\text{Ti}_3\text{C}_2\text{T}_x$ -incorporated GCE for distinct investigation of a) Pb^{2+} as of 0.10–0.55 mM; b) Cd^{2+} as of 0.1–1.0 mM; c) Cu^{2+} as of 0.1–1.4 mM; d) Hg^{2+} as of 1.0–1.9 mM. Insets within board (a–d) are the conforming linear standardization schemes of peak current against Pb^{2+} , Cd^{2+} , Cu^{2+} , and Hg^{2+} absorptions, correspondingly. Reproduced with permission.^[91] Copyright 2017, Elsevier Ltd.

limit and exactness are more vulnerable than MMA (Figure 16h). Additionally, it may represent the linear connection for MMA within the capacity from 10^{-1} nm via $\gamma = -10.36 - 1.3 \log C$. The calculated recognition limit is 6.61 am, a valuable complement and development for other ultrasensitive detection techniques (Figure 16i).

The essential edge of MXene for SERS implementations is the possibility to thrill hot locations within the visible and NIR spectra. Similarly, to noble metals, both physical and chemical enhancements occur. The method of assembling hot places due to interband change to the vacant energy forms of the functional group and charge transfer to the probe molecule offers a synergetic improvement of both electric field and chemical improvement.^[96]

4.5.2. Drug Delivery

Conventional drug administration requires high drug dosages to achieve therapeutic levels, resulting in resistance to various medicines or drugs and poisonousness to normal cells and tissues.^[97] Therefore, nanomaterials that act as delivery agents in particular tissues through capturing specific drugs are required.^[17b] MXene-based NMs have emerged as drug carriers for precision

treatment as they possess negatively charged surfaces, rich surface functional groups, and planar structures. Very thin modified Ti_3C_2 nanosheets can be easily transported throughout blood vessels,^[9b] while the large surface area facilitates the potential coating of DOX and effectively eradicates tumor cells by high drug-releasing ability in an acidic medium.^[17b]

Sandwich-like $\text{Ti}_3\text{C}_2@Au$ nanorods (GNRs)/polydopamine (PDA)/ Ti_3C_2 NC were designed^[98] via an in situ growth method which displayed high drug loading efficiency and improved photothermal conversion proficiency. For further evaluation, as-synthesized NC DOX was taken as a representative drug to evaluate the drug-loaded capacity and pH/NIR responsive performance of $\text{Ti}_3\text{C}_2@Au$ nanorods/PDA/ Ti_3C_2 NC. The drug loading capacity touched 95.88%. The reason behind such enhanced drug doping ability was the high surface area. In addition, strong electrostatic interactions between negatively charged NC and positively charged DOX also improve the drug loading ability of the NMs.

Beibei et al.^[98] found a type of sandwich-similar Ti_3C_2 MXene-based nanoplatform $\text{Ti}_3\text{C}_2@GNRs/PDA/Ti_3C_2$ with elevated drug-incorporating efficiency, superior photothermal modification effectiveness, and pH/NIR sensitivity included by facile growth process, electrostatic, and physical adsorption relations (Figure 17a). The structure of the Ti_3C_2 nanofilms also would

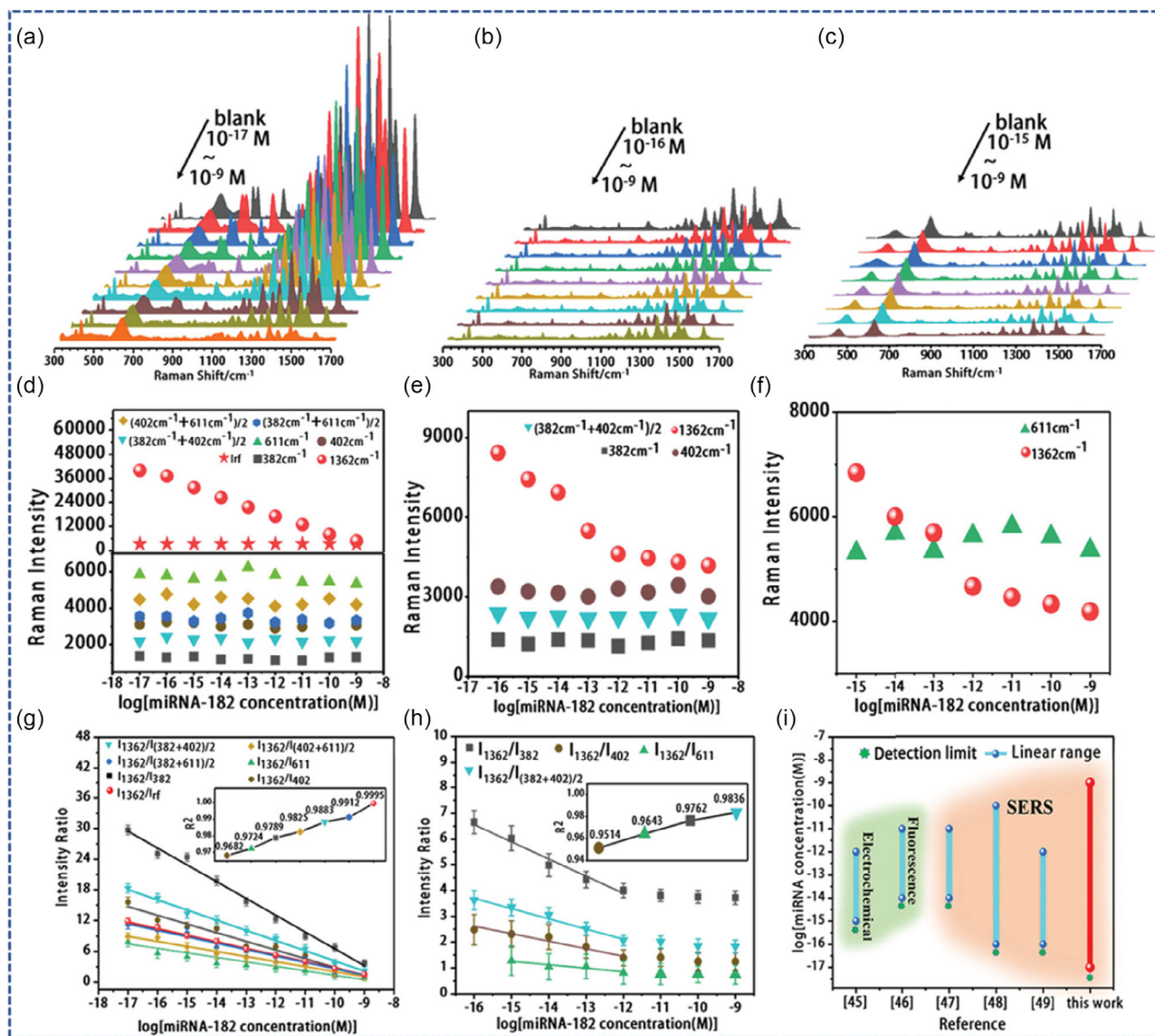


Figure 16. a) SERS spectra of MMA in detecting miRNA-182 with distinct absorptions, b) SERS spectra of MoS₂@AuNPs in seeing miRNA-182 with typical absorptions, and c) SERS spectra of MXene@AuNPs within the recognition of miRNA-182 with diverse absorptions. The scopes of the Y axis in (a–c) are identical from 0 to 45 000. d) Illustration of the SERS intensities of MMA at 382, 402, 611, and 1362 cm⁻¹, e) MoS₂@AuNPs at 382, 402, and 1362 cm⁻¹, and f) MXene@AuNPs at 611 and 1362 cm⁻¹. g) Scatters and fit arcs of ratio metric value developed from MMA within detecting miRNA-182 with distinct absorptions. The inset shows scattered plots of fit coefficient R² of particular ratio metric matters. h) Scatters and fit arcs of ratio metric value developed from MoS₂@AuNPs and I1362/I611 yielded from MXene@AuNPs in detecting miRNA-182 with distinct absorptions. i) The acquired outcomes and other consequences reported for microRNA-182 recognition. Reproduced with permission.^[95] Copyright 2020, John Wiley and Sons.

be monitored from TEM pictures, as shown in Figure 17b. A single-layer nanofilm would be kept in the heightened TEM picture of Ti₃C₂ nanofilms (Insert view of Figure 17b). Figure 17c shows TEM pictures of Ti₃C₂@GNRs after the facile growth strategy. We could find it from the connected elaborated TEM pictures of Ti₃C₂@GNRs (inset view of Figure 17c) where GNRs are arranged in conditions on Ti₃C₂ nanofilms showing the profitable growth of GNRs on the consistency of Ti₃C₂ nanofilms. Moreover, Figure 17d shows that there were Ti₃C₂ nanofilms upon the exterior of Ti₃C₂@GNRs. As shown in Figure 17e, the lateral extent of Ti₃C₂@GNRs was around

120 nm, and the width of Ti₃C₂@GNRs was typically dispersed between 15.2 and 23.4 nm. Figure 17f shows the adjacent area of Ti₃C₂@GNRs/PDA/Ti₃C₂ enlarged to around 250 nm, and the elevation widened from 17.4 to 25.3 nm.

MXene-based NMs were incorporated with hydrogels to control the drug release rate effectively. Chronic wound healing is a significant issue in healthcare fields. Yang et al.^[99] fabricated MXene-based hydrogel structure that acts as a magnetic- and photo-sensitive drug delivery agent for repairing deep chronic wounds using a modified Stöber process. The NC comprises poly(*N*-isopropyl acrylamide)-alginate dual-system hydrogels

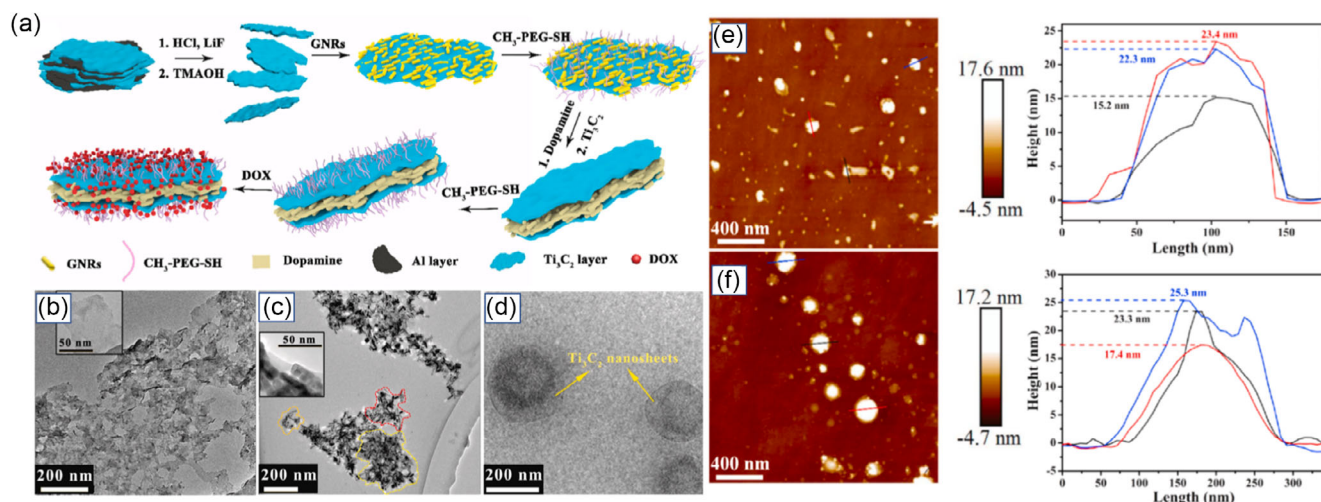


Figure 17. a) Graphic illustration for the synthesis of Ti_3C_2 @GNRs/PDA/ Ti_3C_2 . b) Ti_3C_2 nanofilms, c) Ti_3C_2 @GNRs, and d) Ti_3C_2 @GNRs/PDA/ Ti_3C_2 . (inset descriptions of b and c: the exaggerated TEM pictures of Ti_3C_2 nanofilms and Ti_3C_2 @GNRs, correspondingly). AFM pictures and height shapes of e) Ti_3C_2 @GNRs and f) Ti_3C_2 @GNRs/PDA/ Ti_3C_2 . Reproduced with permission.^[98] Copyright 2021, Elsevier Ltd.

and MXene-wrapped magnetic colloids. It exhibits controllable drug delivery capacity, less poisonous side effects of drugs, minimizes bacterial infection, and supports wound healing procedures. It applied the practical application of the as-synthesized MXene-based hydrogel system to the rat's full-width cutaneous and hypodermic wound. In vivo assessed the hydrogel system with open and epidermal skin wounds of diabetic mice. Infection is the most general risk to the healing of chronic wounds. The MXene-based hydrogel system showed a potential damage closer rate in rats without transferring bacterial infections.

Mycobacterium tuberculosis is considered one of the most hazardous pathogenic bacteria, which causes a severe illness called *tuberculosis*. A nanobiosensor was developed by Zhang et al.^[100] to effectively detect *M. tuberculosis* using Ti_3C_2 MXene to amplify the signals that act as transduction material, a probe of nucleic acid, particularly 16s rDNA portion of *M. tuberculosis* H37Ra that acts as a target biomarker. There were strong interactions between Zr crosslinked Ti_3C_2 MXene and phosphate groups of the target fragments, which resulted in a direct linkage of Ti_3C_2 MXene and target segments Table 2. This biosensor provides potential detection of *M. tuberculosis*.^[101]

5. Advantages of 2D MXenes for Biomedical Application over Other Types of Nanomaterials

1) MXenes are usually fabricated by inert metals combined with carbonitrides which makes their functioning ecofriendly during cell proliferation and differentiation processes.^[47] 2) MXene-based NMs possesses large active surface area and hydrophilicity which enhance drug-loading capacity and adsorption of biomolecules. Therefore, they can be used as effective material for biosensing.^[112] 3) MXene-based NMs are nontoxic and biocompatible, so, they have less side effects without any requirement of surface coating biocompatible materials.^[113] 4) Although graphene^[114] and black phosphorous^[115] are successfully utilized as biomedical

agents; however, these still remains as academic interested materials, and only few practical applications have been studied.^[113] 5) Ferromagnetism makes MXenes suitable for MRI while light absorption capacity of MXenes in NIR regions makes them suitable materials for PTT and PA imaging.

6. Conclusion, Challenges, and Future Outlook

In conclusion, MXene-based NMs, as a recent component of 2D NMs, were initially found by Gogotsi and co-workers in 2011. Dissimilar from conventional 2D NMs, the initial configurations of MXenes, like transition metal carbides, nitrides, and carbonitrides, only require in situ synthesis strategies with etching coatings of MAX at ambient temperature. Similarly, it has been broadly noted that MXene-based NMs have numerous remarkable features, like sizeable exact surface area, excessively low cytotoxicity, affluent surface functional groups, and unique electronic, mechanical, and physicochemical effects. Nonetheless, even with an in-depth analysis of MXene-based NMs, these remarkable characteristics cannot fulfil the essentials for different utilizations. Thus, surface transformation and functionalization are essential to improve MXene-based nanomaterials' effects. Behind surface incorporation, MXene-based nanomaterials have drawn much concentration. These have been broadly involved in multiple implementations, like biomedicine, energy, and the atmosphere. The biomedical utilization of MXene-based NMs for biosensing, drug delivery design, theragnostic nanoplatform, and sterile agents has been outlined and examined in detail.

Undoubtedly, multiple distinctive challenges occur in using 2D MXenes for conversion utilizations like commercial purposes, design control, proposed superficial engineering, and long-term biocompatibility assessment. In addition, 2D MXene NMs have biomedical applications like stem cell engineering, regenerative treatment, gene medicine, tissue engineering, and perhaps other new cancer therapies. It is positively predicted that the significant and multidisciplinary-joint actions will enable a mechanistic

Table 2. Various types of MXene-based NMs in biosensing, drug delivery, and other biomedical applications along with their synthesis methods.

MXene-based NMs	Linear range	Limit of detection	Preparation method	Application	Detailed application	References
Ti ₃ C ₂ -MXene	0.0001–2000 ngmL ⁻¹	–	Minimally intensive layer delamination	Biosensor	Detection of carcinoembryonic antigen	[102]
Poly-l-lysine/glucose oxidase/Ti ₃ C ₂	4.0–20 μM	2.6 μM	LiF + HCl etching	Biosensor	Detection of H ₂ O ₂	[103]
Ti ₃ C ₂ /polyacrylamide	–	–	In situ free radical polymerization	Drug delivery	97.5–127.7 mg g ⁻¹ drug loading ability and percentage releases 62.1–81.4%	[27]
Cellulose/DOX/Ti ₃ C ₂ MXene	235.2–313.6 ppm	–	HF etching	Drug delivery	Chemotherapeutic agent, synergistic chemotherapy and PTT with power density of 1.0 W cm ⁻²	[10a]
Glucose oxidase /Au/MXene/ Nafion	0.1–18 mM	5.9 μM	–	Biosensor	Detection of glucose	[89]
TiO ₂ -Ti ₃ C ₂ /Hemoglobin/ Nafion	0.1–380 μM	14 nM	Hydrothermal method	Biosensor	Detection of H ₂ O ₂	[104]
Ti ₃ C ₂ -graphene oxide	2 μM–1 mM	1.95 μM	LiF/HCl-etching	Biosensor	Detection of H ₂ O ₂	[105]
Ti ₃ C ₂ T _x /Pt NPs	–	448 nM	Etching of aluminum layer	Biosensor	Detection of H ₂ O ₂	[106]
Ti ₃ C ₂ T _x /Prussian blue	200 × 10 ⁻⁹ –4.8 × 10 ⁻³ M	67 × 10 ⁻⁹ M	Minimally intensive layer delamination	Biosensor	Detection of glucose	[107]
ZnO tetrapods/MXene	0.05–0.7 mM	17 μM	LiF + HCl etching	Biosensor	Detection of glucose	[108]
Ti ₃ C ₂ T _x MXene	–	–	Ultrasonication	Antibacterial activity	Inhibits the growth of E. coli and B. subtilis	[22a]
Ti ₃ C ₂ T _x /polyvinylidene fluoride	–	–	Vacuum-assisted filtration	Antibacterial activity	Inhibits the growth of E. coli and B. subtilis	[10b]
Ti ₃ C ₂ -MXene	–	–	HF etching	Biosensor	Detection of dopamine	[109]
Ti ₃ C ₂ -MXene/Hb	0.1–260 μM	20 nM	HF etching	Biosensor	Detection of H ₂ O ₂	[110]
Ti ₃ C ₂ -MXene/Hb	0.5–11 800 μM	0.12 μM	–	Biosensor	Detection of NaNO ₂	[111]

interpretation of MXene-based strategies for nanomedicine. This will allow advanced paradigms to be more quickly and broadly utilized in adaptable biomedicine.

Although MXenes possess unique properties and have demonstrated significant potential for biomedical applications, there are still numerous challenges to their clinical translation. The persistent biosafety of MXenes has not been systematically evaluated. However, various investigations have exhibited that presently known MXenes for biomedical utilization are typically biocompatible, and few are biodegradable *in vivo*.^[26,56,68] Most of these investigations were based on cell experimentations or short-term hematological assays. Further biomedical applications will require methodological studies on the biosafety of MXenes.

The biomedical utilization of 2D MXenes has been restricted through their comfortable accumulation, complex surface engineering, inadequate strength, and possible toxicity. The sideways size, the number of layers, and the extent of oxidation affect the degradation and stability during *in vivo* circulation. The interactions between the physiological atmosphere and nanofilms, the metabolic pathway analysis, and the side effects of MXene nanofilms have not been described yet. There is a tremendous

contradiction that quick degradation can affect the expected therapeutic results. In comparison, the degradation meets the necessities of biological protection. Thus, a suitable degradation rate should be considered during the configuration and preparation of MXenes to seek ideal therapeutic results and low toxicity.

Although numerous investigations have shown the great possibility of MXenes in oncological implementations, their clinical translation is yet in its infancy. Thus, in subsequent basic research, we should systematically study the interaction between MXenes and biological microenvironments. Further clarification needs further explanation on the impact of surface functionalization on the natural behavior of MXenes. The scale-up incorporation of 2D MXenes is significant due to their structure and engineering. A different and more in-depth investigation of material science and clinical translation needs association with investigators of interdisciplinary and industrial areas. It is appreciatively expected that the development of nanotechnology and bioscience could achieve more fundamental and technological breakthroughs to afford the infinite application of MXenes in various biomedical areas soon, delivering the main challenges and critical issues satisfactorily solved.

2D MXenes have been broadly explored in biomedical applications, and these outcomes preliminarily indicate that they have low poisonousness, while the poisonousness of 2D MXenes and active 2D MXenes in the atmosphere and human beings has still not been systematically investigated. Thus, it is essential to clarify the toxicity performance of 2D MXenes and the functioning of 2D MXenes in atmospheric applications. These consequences propose an anti-inflammatory impact produced through $Ti_3C_2T_x$. However, additional investigations are required to illuminate whether the smaller level of distinct cytokines followed in Th cells and monocytes (e.g., TNF- α) would be due to direct impact of $Ti_3C_2T_x$ upon cells.

Acknowledgements

The authors acknowledge support from the Department of Chemistry and Research & development Cell of Maharishi Markandeshwar (Deemed to be University), Mullana, Ambala, Haryana, India.

Conflict of Interest

The authors declare no conflict of interest.

Keywords

biosensors, cancer theranostics, drug delivery, MXene-based nanomaterials, tissue engineering

Received: September 12, 2022
Published online:

- [1] M. Naguib, M. Kurtoglu, V. Presser, J. Lu, J. Niu, M. Heon, L. Hultman, Y. Gogotsi, M. W. Barsoum, *Adv. Mater.* **2011**, *23*, 4248.
- [2] a) B. Anasori, M. R. Lukatskaya, Y. Gogotsi, *Nat. Rev. Mater.* **2017**, *2*, 16098; b) S. S. Siwal, K. Sheoran, K. Mishra, H. Kaur, A. K. Saini, V. Saini, D.-V. N. Vo, H. Y. Nezhad, V. K. Thakur, *Chemosphere* **2022**, *293*, 133542.
- [3] a) L. Bai, W. Yi, T. Sun, Y. Tian, P. Zhang, J. Si, X. Hou, J. Hou, *J. Mater. Chem. B* **2020**, *8*, 6402; b) L. Ding, L. Li, Y. Liu, Y. Wu, Z. Lu, J. Deng, Y. Wei, J. Caro, H. Wang, *Nat. Sustainability* **2020**, *3*, 296; c) Z. Lu, Y. Wei, J. Deng, L. Ding, Z.-K. Li, H. Wang, *ACS Nano* **2019**, *13*, 10535.
- [4] a) K. Sheoran, H. Kaur, S. S. Siwal, A. K. Saini, D.-V. N. Vo, V. K. Thakur, *Chemosphere* **2022**, *299*, 134364; b) H. Kaur, V. K. Thakur, S. S. Siwal, *Mater. Today: Proc.* **2022**, *56*, 112; c) S. Karamveer, V. K. Thakur, S. S. Siwal, *Mater. Today: Proc.* **2022**, *56*, 9.
- [5] a) K. Mishra, V. Kumar Thakur, S. Singh Siwal, *Mater. Today: Proc.* **2022**, *56*, 107; b) S. S. Siwal, Q. Zhang, C. Sun, V. K. Thakur, *Nanomaterials* **2019**, *10*, 2.
- [6] S. S. Siwal, W. Yang, Q. Zhang, *J. Energy Chem.* **2020**, *51*, 113.
- [7] a) M. Khazaei, A. Mishra, N. S. Venkataramanan, A. K. Singh, S. Yunoki, *Curr. Opin. Solid State Mater. Sci.* **2019**, *23*, 164; b) K. S. Novoselov, A. Mishchenko, A. Carvalho, A. H. Castro Neto, *Science* **2016**, *353*, aac9439.
- [8] a) M. W. Barsoum, *Prog. Solid State Chem.* **2000**, *28*, 201; b) V. S. Sivasankarapillai, A. K. Somakumar, J. Joseph, S. Nikazar, A. Rahdar, G. Z. Kyzas, *Nano-Struct. Nano-Objects* **2020**, *22*, 100457.
- [9] a) Z.-K. Li, Y. Wei, X. Gao, L. Ding, Z. Lu, J. Deng, X. Yang, J. Caro, H. Wang, *Angew. Chem., Int. Ed.* **2020**, *59*, 9751; b) H. Lin, X. Wang, L. Yu, Y. Chen, J. Shi, *Nano Lett.* **2017**, *17*, 384; c) H. Lin, S. Gao, C. Dai, Y. Chen, J. Shi, *J. Am. Chem. Soc.* **2020**, *142*, 10567; d) Z. Liu, H. Lin, M. Zhao, C. Dai, S. Zhang, W. Peng, Y. Chen, *Theranostics* **2018**, *8*, 1648; e) X. Han, J. Huang, H. Lin, Z. Wang, P. Li, Y. Chen, *Adv. Healthcare Mater.* **2018**, *7*, 1701394.
- [10] a) C. Xing, S. Chen, X. Liang, Q. Liu, M. Qu, Q. Zou, J. Li, H. Tan, L. Liu, D. Fan, H. Zhang, *ACS Appl. Mater. Interfaces* **2018**, *10*, 27631; b) K. Rasool, K. A. Mahmoud, D. J. Johnson, M. Helal, G. R. Berdiyev, Y. Gogotsi, *Sci. Rep.* **2017**, *7*, 1598.
- [11] R. P. Pandey, K. Rasool, V. E. Madhavan, B. Aïssa, Y. Gogotsi, K. A. Mahmoud, *J. Mater. Chem. A* **2018**, *6*, 3522.
- [12] a) L. Wu, X. Lu, . Dhanjai, Z.-S. Wu, Y. Dong, X. Wang, S. Zheng, J. Chen, *Biosens. Bioelectron.* **2018**, *107*, 69; b) G. P. Lim, C. F. Soon, N. L. Ma, M. Morsin, N. Nayan, M. K. Ahmad, K. S. Tee, *Environ. Res.* **2021**, *201*, 111592; c) H. Kaur, S. S. Siwal, G. Chauhan, A. K. Saini, A. Kumari, V. K. Thakur, *Chemosphere* **2022**, *304*, 135182.
- [13] M. Malaki, A. Maleki, R. S. Varma, *J. Mater. Chem. A* **2019**, *7*, 10843.
- [14] K. Huang, Z. Li, J. Lin, G. Han, P. Huang, *Chem. Soc. Rev.* **2018**, *47*, 5109.
- [15] C. Yang, Y. Luo, H. Lin, M. Ge, J. Shi, X. Zhang, *ACS Nano* **2021**, *15*, 1086.
- [16] H. Lin, Y. Chen, J. Shi, *Adv. Sci.* **2018**, *5*, 1800518.
- [17] a) B. Shao, Z. Liu, G. Zeng, H. Wang, Q. Liang, Q. He, M. Cheng, C. Zhou, L. Jiang, B. Song, *J. Mater. Chem. A* **2020**, *8*, 7508; b) A. Zamhuri, G. P. Lim, N. L. Ma, K. S. Tee, C. F. Soon, *BioMed. Eng. OnLine* **2021**, *20*, 33.
- [18] a) Y.-H. Lee, X.-Q. Zhang, W. Zhang, M.-T. Chang, C.-T. Lin, K.-D. Chang, Y.-C. Yu, J. T.-W. Wang, C.-S. Chang, L.-J. Li, T.-W. Lin, *Adv. Mater.* **2012**, *24*, 2320; b) K.-K. Liu, W. Zhang, Y.-H. Lee, Y.-C. Lin, M.-T. Chang, C.-Y. Su, C.-S. Chang, H. Li, Y. Shi, H. Zhang, C.-S. Lai, L.-J. Li, *Nano Lett.* **2012**, *12*, 1538; c) X. Lu, M. I. B. Utama, J. Lin, X. Gong, J. Zhang, Y. Zhao, S. T. Pantelides, J. Wang, Z. Dong, Z. Liu, W. Zhou, Q. Xiong, *Nano Lett.* **2014**, *14*, 2419.
- [19] a) F. Lei, Y. Sun, K. Liu, S. Gao, L. Liang, B. Pan, Y. Xie, *J. Am. Chem. Soc.* **2014**, *136*, 6826; b) Z. Sun, T. Liao, Y. Dou, S. M. Hwang, M.-S. Park, L. Jiang, J. H. Kim, S. X. Dou, *Nat. Commun.* **2014**, *5*, 3813; c) Y. Sun, F. Lei, S. Gao, B. Pan, J. Zhou, Y. Xie, *Angew. Chem., Int. Ed.* **2013**, *52*, 10569.
- [20] X. Wang, H. Feng, Y. Wu, L. Jiao, *J. Am. Chem. Soc.* **2013**, *135*, 5304.
- [21] B. Yang, Y. Chen, J. Shi, *Chem* **2018**, *4*, 1284.
- [22] a) K. Rasool, M. Helal, A. Ali, C. E. Ren, Y. Gogotsi, K. A. Mahmoud, *ACS Nano* **2016**, *10*, 3674; b) C. Dai, H. Lin, G. Xu, Z. Liu, R. Wu, Y. Chen, *Chem. Mater.* **2017**, *29*, 8637; c) A. Szuplewska, D. Kulpińska, A. Dybko, A. M. Jastrzębska, T. Wojciechowski, A. Rozmysłowska, M. Chudy, I. Grabowska-Jadach, W. Ziemkowska, Z. Brzózka, A. Olszyna, *Mater. Sci. Eng., C* **2019**, *98*, 874.
- [23] F. Shahzad, M. Alhabeib, B. Hatter Christine, B. Anasori, S. Man Hong, M. Koo Chong, Y. Gogotsi, *Science* **2016**, *353*, 1137.
- [24] M. Khazaei, A. Ranjbar, M. Arai, S. Yunoki, *Phys. Rev. B* **2016**, *94*, 125152.
- [25] L. Xiu, Z. Wang, M. Yu, X. Wu, J. Qiu, *ACS Nano* **2018**, *12*, 8017.
- [26] G. Liu, J. Zou, Q. Tang, X. Yang, Y. Zhang, Q. Zhang, W. Huang, P. Chen, J. Shao, X. Dong, *ACS Appl. Mater. Interfaces* **2017**, *9*, 40077.
- [27] P. Zhang, X.-J. Yang, P. Li, Y. Zhao, Q. J. Niu, *Soft Matter* **2020**, *16*, 162.
- [28] X. Lin, Z. Li, J. Qiu, Q. Wang, J. Wang, H. Zhang, T. Chen, *Biomater. Sci.* **2021**, *9*, 5437.

- [29] H. Zou, B. He, P. Kuang, J. Yu, K. Fan, *ACS Appl. Mater. Interfaces* **2018**, *10*, 22311.
- [30] S. S. Siwal, A. K. Saini, S. Rarotra, Q. Zhang, V. K. Thakur, *J. Nanostruct. Chem.* **2021**, *11*, 93.
- [31] a) S. Siwal, N. Devi, V. K. Perla, S. K. Ghosh, K. Mallick, *Catal. Struct. React.* **2019**, *5*, 1; b) S. Samarjeet, G. Sarit, N. Debkumar, D. Nishu, K. P. Venkata, B. Rasmita, M. Kaushik, *Mater. Res. Express* **2017**, *4*, 095306; c) S. Siwal, N. Devi, V. Perla, R. Barik, S. Ghosh, K. Mallick, *Mater. Res. Innovations* **2018**, *23*, 440.
- [32] G. Gao, G. Ding, J. Li, K. Yao, M. Wu, M. Qian, *Nanoscale* **2016**, *8*, 8986.
- [33] L. Gao, C. Li, W. Huang, S. Mei, H. Lin, Q. Ou, Y. Zhang, J. Guo, F. Zhang, S. Xu, H. Zhang, *Chem. Mater.* **2020**, *32*, 1703.
- [34] A. D. Dillon, M. J. Ghidui, A. L. Krick, J. Griggs, S. J. May, Y. Gogotsi, M. W. Barsoum, A. T. Fafarman, *Adv. Funct. Mater.* **2016**, *26*, 4162.
- [35] X. Gao, Z. Jia, B. Wang, X. Wu, T. Sun, X. Liu, Q. Chi, G. Wu, *Chem. Eng. J.* **2021**, *419*, 130019.
- [36] K. Rasool, R. P. Pandey, P. A. Rasheed, S. Buczek, Y. Gogotsi, K. A. Mahmoud, *Mater. Today* **2019**, *30*, 80.
- [37] a) E. Mostafavi, S. Irvani, *Nano-Micro Lett.* **2022**, *14*, 130; b) S. Y. Tee, E. Ye, C. P. Teng, Y. Tanaka, K. Y. Tang, K. Y. Win, M.-Y. Han, *Nanoscale* **2021**, *13*, 14268; c) A. Murali, G. Lokhande, K. A. Deo, A. Brokesh, A. K. Gaharwar, *Mater. Today* **2021**, *50*, 276.
- [38] G. Wang, *J. Phys. Chem. C* **2016**, *120*, 18850.
- [39] C. Si, J. Zhou, Z. Sun, *ACS Appl. Mater. Interfaces* **2015**, *7*, 17510.
- [40] L. Hu, X. Wu, J. Yang, *Nanoscale* **2016**, *8*, 12939.
- [41] X. Zhan, C. Si, J. Zhou, Z. Sun, *Nanoscale Horiz.* **2020**, *5*, 235.
- [42] A. Parihar, A. Singhal, N. Kumar, R. Khan, M. A. Khan, A. K. Srivastava, *Nano-Micro Lett.* **2022**, *14*, 100.
- [43] a) Q. Yang, H. Yin, T. Xu, D. Zhu, J. Yin, Y. Chen, X. Yu, J. Gao, C. Zhang, Y. Chen, Y. Gao, *Small* **2020**, *16*, 1906814; b) G. P. Awasthi, B. Maharjan, S. Shrestha, D. P. Bhattarai, D. Yoon, C. H. Park, C. S. Kim, *Colloids Surf., A* **2020**, *586*, 124282.
- [44] L. Mao, S. Hu, Y. Gao, L. Wang, W. Zhao, L. Fu, H. Cheng, L. Xia, S. Xie, W. Ye, Z. Shi, G. Yang, *Adv. Healthcare Mater.* **2020**, *9*, 2000872.
- [45] a) N. Au - Driscoll, K. Au - Maleski, A. G. Au - Richardson, B. Au - Murphy, B. Au - Anasori, T. H. Au - Lucas, Y. Au - Gogotsi, F. Au - Vitale, *JoVE* **2020**, *12*, e60741; b) H. Rastin, B. Zhang, A. Mazinani, K. Hassan, J. Bi, T. T. Tung, D. Losic, *Nanoscale* **2020**, *12*, 16069.
- [46] a) A. Rafeerad, W. Yan, G. L. Sequiera, N. Sareen, E. Abu-El-Rub, M. Moudgil, S. Dhingra, *Adv. Healthcare Mater.* **2019**, *8*, 1970067; b) G. Ye, Z. Wen, F. Wen, X. Song, L. Wang, C. Li, Y. He, S. Prakash, X. Qiu, *Theranostics* **2020**, *10*, 2047.
- [47] S. Irvani, R. S. Varma, *Mater. Adv.* **2021**, *2*, 2906.
- [48] R. Huang, X. Chen, Y. Dong, X. Zhang, Y. Wei, Z. Yang, W. Li, Y. Guo, J. Liu, Z. Yang, H. Wang, L. Jin, *ACS Appl. Bio Mater.* **2020**, *3*, 2125.
- [49] J. Yin, S. Pan, X. Guo, Y. Gao, D. Zhu, Q. Yang, J. Gao, C. Zhang, Y. Chen, *Nano-Micro Lett.* **2021**, *13*, 30.
- [50] S. Pan, J. Yin, L. Yu, C. Zhang, Y. Zhu, Y. Gao, Y. Chen, *Adv. Sci.* **2020**, *7*, 1901511.
- [51] Y. Fu, J. Zhang, H. Lin, A. Mo, *Mater. Sci. Eng., C* **2021**, *118*, 111367.
- [52] K. Chen, Y. Chen, Q. Deng, S.-H. Jeong, T.-S. Jang, S. Du, H.-E. Kim, Q. Huang, C.-M. Han, *Mater. Lett.* **2018**, *229*, 114.
- [53] Y. Zhu, Z. Wang, R. Zhao, Y. Zhou, L. Feng, S. Gai, P. Yang, *ACS Nano* **2022**, *16*, 3105.
- [54] a) G. Jamalipour Soufi, P. Irvani, A. Hekmatnia, E. Mostafavi, M. Khatami, S. Irvani, *Comments Inorg. Chem.* **2022**, *42*, 174; b) A. Liu, Y. Liu, G. Liu, A. Zhang, Y. Cheng, Y. Li, L. Zhang, L. Wang, H. Zhou, J. Liu, H. Wang, *Chem. Eng. J.* **2022**, *448*, 137691.
- [55] X. Ren, M. Huo, M. Wang, H. Lin, X. Zhang, J. Yin, Y. Chen, H. Chen, *ACS Nano* **2019**, *13*, 6438.
- [56] X. Yu, X. Cai, H. Cui, S.-W. Lee, X.-F. Yu, B. Liu, *Nanoscale* **2017**, *9*, 17859.
- [57] X. Li, F. Liu, D. Huang, N. Xue, Y. Dang, M. Zhang, L. Zhang, B. Li, D. Liu, L. Wang, H. Liu, X. Tao, *Adv. Funct. Mater.* **2020**, *30*, 2000308.
- [58] Y. Liu, Q. Han, W. Yang, X. Gan, Y. Yang, K. Xie, L. Xie, Y. Deng, *Mater. Sci. Eng., C* **2020**, *116*, 111212.
- [59] Z. Liu, M. Zhao, H. Lin, C. Dai, C. Ren, S. Zhang, W. Peng, Y. Chen, *J. Mater. Chem. B* **2018**, *6*, 3541.
- [60] L. Zong, H. Wu, H. Lin, Y. Chen, *Nano Res.* **2018**, *11*, 4149.
- [61] C. Dai, Y. Chen, X. Jing, L. Xiang, D. Yang, H. Lin, Z. Liu, X. Han, R. Wu, *ACS Nano* **2017**, *11*, 12696.
- [62] Z. Hao, Y. Li, X. Liu, T. Jiang, Y. He, X. Zhang, C. Cong, D. Wang, Z. Liu, D. Gao, *Chem. Eng. J.* **2021**, *425*, 130639.
- [63] C. Korupalli, K.-L. You, G. Getachew, A. S. Rasal, W. B. Dirersa, M. Zakki Fahmi, J.-Y. Chang, *Pharmaceutics* **2022**, *14*, 304.
- [64] Y. Xu, Y. Wang, J. An, A. C. Sedgwick, M. Li, J. Xie, W. Hu, J. Kang, S. Sen, A. Steinbrueck, B. Zhang, L. Qiao, S. Wageh, J. F. Arambula, L. Liu, H. Zhang, J. L. Sessler, J. S. Kim, *Bioact. Mater.* **2022**, *14*, 76.
- [65] X. Han, X. Jing, D. Yang, H. Lin, Z. Wang, H. Ran, P. Li, Y. Chen, *Theranostics* **2018**, *8*, 4491.
- [66] W. Tang, Z. Dong, R. Zhang, X. Yi, K. Yang, M. Jin, C. Yuan, Z. Xiao, Z. Liu, L. Cheng, *ACS Nano* **2019**, *13*, 284.
- [67] J. Shao, J. Zhang, C. Jiang, J. Lin, P. Huang, *Chem. Eng. J.* **2020**, *400*, 126009.
- [68] H. Lin, S. Gao, C. Dai, Y. Chen, J. Shi, *J. Am. Chem. Soc.* **2017**, *139*, 16235.
- [69] W. Feng, R. Wang, Y. Zhou, L. Ding, X. Gao, B. Zhou, P. Hu, Y. Chen, *Adv. Funct. Mater.* **2019**, *29*, 1901942.
- [70] S. S. Siwal, Q. Zhang, A. K. Saini, V. K. Thakur, *J. Renewable Mater.* **2020**, *8*, 1543.
- [71] a) S. S. Siwal, G. Chaudhary, A. K. Saini, H. Kaur, V. Saini, S. K. Mokhta, R. Chand, U. K. Chandel, G. Christie, V. K. Thakur, *J. Environ. Chem. Eng.* **2021**, *9*, 106284; b) H. Kaur, S. S. Siwal, P. Bishnoi, S. Rarotra, D.-V. N. Vo, V. K. Gupta, D. Robert, K. Vijay, *Biomater. Polym. Horiz.* **2022**, *1*.
- [72] a) C. Weiss, M. Carriere, L. Fusco, I. Capua, J. A. Regla-Nava, M. Pasquali, J. A. Scott, F. Vitale, M. A. Unal, C. Mattevi, D. Bedognetti, A. Merkoçi, E. Tasciotti, A. Yilmazer, Y. Gogotsi, F. Stellacci, L. G. Delogu, *ACS Nano* **2020**, *14*, 6383; b) P. K. Rai, Z. Usmani, V. K. Thakur, V. K. Gupta, Y. K. Mishra, *Curr. Res. Green Sustainable Chem.* **2020**, *3*, 100011; c) V. Palmieri, M. Papi, *Nano Today* **2020**, *33*, 100883.
- [73] a) W. Sun, F.-G. Wu, *Chem. – Asian J.* **2018**, *13*, 3378; b) C. Martín, K. Kostarelos, M. Prato, A. Bianco, *Chem. Commun.* **2019**, *55*, 5540; c) A. Gazzì, L. Fusco, A. Khan, D. Bedognetti, B. Zavan, F. Vitale, A. Yilmazer, L. G. Delogu, *Front. Bioeng. Biotechnol.* **2019**, *7*, 295.
- [74] M. A. Unal, F. Bayraktar, L. Fusco, O. Besbinar, C. E. Shuck, S. Yalcin, M. T. Erken, A. Ozkul, C. Gurcan, O. Panatli, G. Y. Summak, C. Gokce, M. Orecchioni, A. Gazzì, F. Vitale, J. Somers, E. Demir, S. S. Yildiz, H. Nazir, J.-C. Grivel, D. Bedognetti, A. Crisanti, K. C. Akcali, Y. Gogotsi, L. G. Delogu, A. Yilmazer, *Nano Today* **2021**, *38*, 101136.
- [75] a) X. Jiang, A. V. Kuklin, A. Baev, Y. Ge, H. Ågren, H. Zhang, P. N. Prasad, *Phys. Rep.* **2020**, *848*, 1; b) S. K. Hwang, S.-M. Kang, M. Rethinasabapathy, C. Roh, Y. S. Huh, *Chem. Eng. J.* **2020**, *397*, 125428.
- [76] T. A. Tabish, M. Z. I. Pranjol, F. Jabeen, T. Abdullah, A. Latif, A. Khalid, M. Ali, H. Hayat, P. G. Winyard, J. L. Whatmore, S. Zhang, *Appl. Mater. Today* **2018**, *12*, 389.
- [77] I. A. Vasyukova, O. V. Zakharova, D. V. Kuznetsov, A. A. Gusev, *Nanomaterials* **2022**, *12*, 1797.
- [78] P. Irvani, S. Irvani, R. S. Varma, *Micromachines* **2022**, *13*, 1383.
- [79] G. K. Nasrallah, M. Al-Asmakh, K. Rasool, K. A. Mahmoud, *Environ. Sci.: Nano* **2018**, *5*, 1002.

- [80] Z. Xu, G. Liu, H. Ye, W. Jin, Z. Cui, *J. Membr. Sci.* **2018**, 563, 625.
- [81] L. Pu, J. Zhang, N. K. L. Jiresse, Y. Gao, H. Zhou, N. Naik, P. Gao, Z. Guo, *Adv. Compos. Hybrid Mater.* **2022**, 5, 356.
- [82] N. Jaya Prakash, B. Kandasubramanian, *J. Alloys Compd.* **2021**, 862, 158547.
- [83] J. Zhang, Y. Fu, A. Mo, *Int. J. Nanomed.* **2019**, 14, 10091.
- [84] J. Huang, Z. Li, Y. Mao, Z. Li, *Nano Select* **2021**, 2, 1480.
- [85] R. D. Nagarajan, A. Sundaramurthy, A. K. Sundramoorthy, *Chemosphere* **2022**, 286, 131478.
- [86] B. Fariba, B. Hadi, *Surf. Eng. Appl. Electrochem.* **2021**, 57, 708.
- [87] R. D. Nagarajan, P. Murugan, K. Palaniyandi, R. Atchudan, A. K. Sundramoorthy, *Micromachines* **2021**, 12, 862.
- [88] F. Zhu, X. Wang, X. Yang, C. Zhao, Y. Zhang, S. Qu, S. Wu, W. Ji, *Anal. Methods* **2021**, 13, 2512.
- [89] R. B. Rakhi, P. Nayak, C. Xia, H. N. Alshareef, *Sci. Rep.* **2016**, 6, 36422.
- [90] Y. Guo, M. Zhong, Z. Fang, P. Wan, G. Yu, *Nano Lett.* **2019**, 19, 1143.
- [91] X. Zhu, B. Liu, H. Hou, Z. Huang, K. M. Zeinu, L. Huang, X. Yuan, D. Guo, J. Hu, J. Yang, *Electrochim. Acta* **2017**, 248, 46.
- [92] P. A. Rasheed, R. P. Pandey, K. Rasool, K. A. Mahmoud, *Sens. Actuators, B* **2018**, 265, 652.
- [93] a) P. Karthick Kannan, P. Shankar, C. Blackman, C.-H. Chung, *Adv. Mater.* **2019**, 31, 1803432; b) Y. Tan, L. Ma, Z. Gao, M. Chen, F. Chen, *Nano Lett.* **2017**, 17, 2621; c) X. Ling, W. Fang, Y.-H. Lee, P. T. Araujo, X. Zhang, J. F. Rodriguez-Nieva, Y. Lin, J. Zhang, J. Kong, M. S. Dresselhaus, *Nano Lett.* **2014**, 14, 3033.
- [94] a) E. Satheeshkumar, T. Makaryan, A. Melikyan, H. Minassian, Y. Gogotsi, M. Yoshimura, *Sci. Rep.* **2016**, 6, 32049; b) A. Sarycheva, T. Makaryan, K. Maleski, E. Satheeshkumar, A. Melikyan, H. Minassian, M. Yoshimura, Y. Gogotsi, *J. Phys. Chem. C* **2017**, 121, 19983; c) B. Soundiraraju, B. K. George, *ACS Nano* **2017**, 11, 8892.
- [95] L. Liu, C. Shangguan, J. Guo, K. Ma, S. Jiao, Y. Yao, J. Wang, *Adv. Opt. Mater.* **2020**, 8, 2001214.
- [96] O. Guselnikova, H. Lim, H.-J. Kim, S. H. Kim, A. Gorbunova, M. Eguchi, P. Postnikov, T. Nakanishi, T. Asahi, J. Na, Y. Yamauchi, *Small* **2022**, 18, 2107182.
- [97] M. van Elk, B. P. Murphy, T. Eufrásio-da-Silva, D. P. O'Reilly, T. Vermonden, W. E. Hennink, G. P. Duffy, E. Ruiz-Hernández, *Int. J. Pharm.* **2016**, 515, 132.
- [98] B. Zhu, J. Shi, C. Liu, J. Li, S. Cao, *Ceram. Int.* **2021**, 47, 24252.
- [99] X. Yang, C. Zhang, D. Deng, Y. Gu, H. Wang, Q. Zhong, *Small* **2022**, 18, 2104368.
- [100] W. Sinshaw, A. Kebede, A. Bitew, E. Tesfaye, M. Tadesse, Z. Mehamed, B. Yenew, M. Amare, B. Dagne, G. Diriba, A. Alemu, M. Getahun, D. Fikadu, K. Desta, H. H. Tola, *BMC Infect. Dis.* **2019**, 19, 641.
- [101] M. Mathew, C. S. Rout, *Curr. Opin. Electrochem.* **2021**, 30, 100782.
- [102] S. Kumar, Y. Lei, N. H. Alshareef, M. A. Quevedo-Lopez, K. N. Salama, *Biosens. Bioelectron.* **2018**, 121, 243.
- [103] M. Wu, Q. Zhang, Y. Fang, C. Deng, F. Zhou, Y. Zhang, X. Wang, Y. Tang, Y. Wang, *J. Colloid Interface Sci.* **2021**, 586, 20.
- [104] F. Wang, C. Yang, M. Duan, Y. Tang, J. Zhu, *Biosens. Bioelectron.* **2015**, 74, 1022.
- [105] J. Zheng, J. Diao, Y. Jin, A. Ding, B. Wang, L. Wu, B. Weng, J. Chen, *J. Electrochem. Soc.* **2018**, 165, B227.
- [106] L. Lorencova, T. Bertok, J. Filip, M. Jerigova, D. Velic, P. Kasak, K. A. Mahmoud, J. Tkac, *Sens. Actuators, B* **2018**, 263, 360.
- [107] Y. Lei, W. Zhao, Y. Zhang, Q. Jiang, J.-H. He, A. J. Baeumner, O. S. Wolfbeis, Z. L. Wang, K. N. Salama, H. N. Alshareef, *Small* **2019**, 15, 1901190.
- [108] V. Myndrul, E. Coy, N. Babayevska, V. Zahorodna, V. Balitskiy, I. Baginskiy, O. Gogotsi, M. Bechelany, M. T. Giardi, I. Iatsunskyi, *Biosens. Bioelectron.* **2022**, 207, 114141.
- [109] B. Xu, M. Zhu, W. Zhang, X. Zhen, Z. Pei, Q. Xue, C. Zhi, P. Shi, *Adv. Mater.* **2016**, 28, 3333.
- [110] F. Wang, C. Yang, C. Duan, D. Xiao, Y. Tang, J. Zhu, *J. Electrochem. Soc.* **2014**, 162, B16.
- [111] H. Liu, C. Duan, C. Yang, W. Shen, F. Wang, Z. Zhu, *Sens. Actuators, B* **2015**, 218, 60.
- [112] A. Srivastava, A. Verma, Y. K. Prajapati, in *Handbook of Nanomaterials for Sensing Applications* (Eds: C. M. Hussain, S. K. Kailasa), Elsevier **2021**.
- [113] A. Sundaram, J. S. Ponraj, C. Wang, W. K. Peng, R. K. Manavalan, S. C. Dhanabalan, H. Zhang, J. Gaspar, *J. Mater. Chem. B* **2020**, 8, 4990.
- [114] C. Xing, G. Jing, X. Liang, M. Qiu, Z. Li, R. Cao, X. Li, D. Fan, H. Zhang, *Nanoscale* **2017**, 9, 8096.
- [115] a) H. Huang, R. Jiang, Y. Feng, H. Ouyang, N. Zhou, X. Zhang, Y. Wei, *Nanoscale* **2020**, 12, 1325; b) Z. Xie, D. Wang, T. Fan, C. Xing, Z. Li, W. Tao, L. Liu, S. Bao, D. Fan, H. Zhang, *J. Mater. Chem. B* **2018**, 6, 4747.



Samarjeet Singh Siwal is currently working as an Associate Professor in the Department of Chemistry, Maharishi Markandeshwar (Deemed to be University), Mullana-India. He received his Ph.D. in Chemistry from the University of Johannesburg, South Africa, in 2017. Then, he moved to Kunming University of Science and Technology (KUST), China as a post-doctoral research fellow. His current research interests include synthesising and applying 2D materials in different fields, such as overall water splitting, supercapacitors, fuel cells and biosensors. He has published over 62 SCI journal articles, 2 patents, and 04 book chapters.



Harjot Kaur is currently carrying-out Doctoral degree (under Dr. Samarjeet Singh Siwal & Professor Vijay Kumar Thakur) at the Department of Chemistry, Maharishi Markandeshwar (Deemed to be University) Mullana, Ambala, India. She received her bachelor's degree in 2017 from Kurukshetra University, Kurukshetra, India. She did her Master's degree in chemistry from Maharishi Markandeshwar (Deemed to be University), Mullana-Ambala, India in 2020. Her research interests focus on developing nanocomposites and nanotechnologies for enhanced biosensing and renewable energy technologies.



Gunjan Chauhan is currently an Assistant Professor in the Department of Chemistry, Maharishi Markandeshwar (Deemed to be University), Mullana-India. She received her M.Phil. and Ph.D. degrees from Himachal Pradesh University, Shimla, and Post-graduated from Panjab University Chandigarh, India. Her area of research interest includes nano-chemistry, enzyme immobilization, catalytic activity, photocatalytic degradation, and antimicrobial activity screening.



Vijay Kumar Thakur is a professor and founding head of the Biorefining and Advanced Materials Research Centre at SRUC, Edinburgh, UK. Before commencing his tenure at SRUC, he previously held faculty positions at Cranfield University, Washington State University, USA, and Nanyang Technological University, Singapore. His research activities span the disciplines of biorefining, chemistry, manufacturing, materials science, nanotechnology, and sustainable and advanced materials. He has published over 350 SCI journal articles, 2 patents, 52 books, and 40 book chapters. He sits on the editorial board of several SCI journals as an editor/editorial advisory board member.